Atmos. Meas. Tech. Discuss., 8, 2013–2065, 2015
www.atmos-meas-tech-discuss.net/8/2013/2015/
doi:10.5194/amtd-8-2013-2015

Atmospheric Measurement Techniques Discussions
Open Access

Synchronous starphotometry and lidar measurements at Eureka in High Canadian Arctic

K. Baibakov[1,2], N. T. O'Neill[1], L. Ivanescu[1], T. J. Duck[3], C. Perro[3], A. Herber[4], K.-H. Schulz[5], and O. Schrems[2,4]

[1]Centre d'Applications et de Recherches en Télédétection, Université de Sherbrooke, Sherbrooke, Canada
[2]Dep. of Chemistry, University of Bremen, Bremen, Germany
[3]Dep. of Physics and Atmospheric Science, Dalhousie University, Halifax, Canada
[4]Alfred Wegener Institute for Polar and Marine Research, Bremerhaven, Germany
[5]Dr. Schulz & Partner GmbH, Buckow, Germany

Received: 24 January 2015 – Accepted: 26 January 2015 – Published: 19 February 2015

Correspondence to: K. Baibakov (k.baibakov@usherbrooke.ca)

Published by Copernicus Publications on behalf of the European Geosciences Union.

Abstract

We present recent progress related to the night-time retrievals of aerosol and cloud optical depth using starphotometry over the PEARL (Polar Environmental Atmospheric Research Laboratory) station at Eureka (Nunavut, Canada) in the High Arctic (80° N, 86° W). In the spring of 2011 and 2012, the SPSTAR starphotometer was employed to acquire aerosol optical depth (AOD) measurements while vertical aerosol and cloud backscatter coefficient profiles were acquired using the CANDAC Raman Lidar (CRL). Several events were detected and characterized using starphotometry-lidar synergy: aerosols (short term aerosol events on 9 and 10 March 2011); a potential multi-night aerosol event across three polar nights (13–15 March 2012), a thin cloud event (21 February 2011) and a very low altitude ice crystals (10 March 2011). Using a simple backscatter coefficient threshold criterion we calculated fine and coarse (sub and super-micron) mode AODs from the vertically integrated CRL profiles. These were compared with their starphotometry analogues produced from a spectral deconvolution algorithm. The process-level analysis showed, in general, good agreement in terms of the physical coherence between high frequency starphotometry and lidar data. We argue that R^2 (coefficient of determination) is the most robust means of comparing lidar and starphotometer data since it is sensitive to significant optico-physical variations associated with these two independent data sources while being minimally dependent on retrieval and calibration artifacts. Differences between the fine and course mode components of the starphotometry and lidar data is clearly also useful but is more dependent on such artifacts. Studying climatological seasonal aerosol trends necessitates effective cloud-screening procedures: temporal and spectral cloud screening of starphotometry data was found to agree moderately well with temporal cloud screening results except in the presence of thin homogeneous cloud. We conclude that better screening conditions can be implemented to arrive at a robust method for combined temporal/spectral cloud-screening of starphotometer (and possibly sunphotometer) data. In general, as our understanding of process-level details increases with

growing datasets, we will inevitably have more confidence in bulk climatological analyses of ground-based and satellite retrievals of aerosol parameters where conditions are less than ideal because of the weakness of the polar winter aerosol signal.

1 Introduction

The Arctic region, often viewed as an early indication system for many aspects of climate change, has been recently undergoing major alterations including alarmingly increasing temperatures, retreating sea-ice cover and record low ozone concentrations in the winter (Moritz et al., 2002; Wang and Key, 2003; Manney et al., 2011; Duarte et al., 2012). The current Global Circulation Models (GCM) underestimate the rate of sea-ice decline (Stroeve et al., 2011) and might differ substantially in terms of their projections (Kattsov and Källén, 2005). The differences between observations and model simulations and the scatter among models are due to the uncertainties in the underlying physical processes. In particular, the lack of understanding associated with a complexity of aerosol and cloud processes remains one of the major obstacles in accurately reproducing and predicting the Arctic climate (Kattsov and Källén, 2005; Inoue et al., 2006).

Aerosols can directly reduce the incoming shortwave radiation reaching the surface. Important examples in the Arctic include the effects of transported biomass burning, forest fire and volcanic plumes (e.g. Stone et al., 2008; Engvall et al., 2009; Young et al., 2012). In addition, aerosols play a profound indirect role serving as condensation nuclei for new clouds and modifying properties of already existing clouds. Understanding the nucleating role of aerosols in mixed-phase type clouds, for example, remains an important problem in the Arctic climate studies (Prenni et al., 2007; Verlinde et al., 2007; McFarquhar et al., 2011). For a particular scene, the net aerosol radiative effect depends on the aerosol type, size, plume height as well as underlying surface albedo and available short-wave radiation.

Because of its unique conditions, the Arctic has been an area of intense interest for aerosol studies. The multi-month daylight and darkness periods, isolated air masses and distinct temperature and humidity regimes result in complex and climatologically important atmospheric phenomena. At the same time, the availability of data, even simple meteorological measurements, is severely limited in the Arctic because of its remoteness and harshness. As a consequence, there are only a few permanent Arctic stations with a continuous track of aerosol measurements. This record is augmented by intensive field campaigns with particular objectives concerning aerosols and aerosol-cloud interactions: e.g. ASTAR (Yamanouchi et al., 2005), ARCTAS (Jacob et al., 2010), ISDAC (McFarquhar et al., 2011).

The synergy of ground-based sunphotometer and lidar instruments has proven to be very effective in aerosol studies during the day-time. Sunphotometers (Shaw, 1983), based on the extinction of solar radiation, provide aerosol optical depth (AOD). AOD is an indicator of total aerosol column concentration and is the most important aerosol radiative parameter. A sunphotometer measures AOD in multiple channels and yields an estimation of particle abundance as well as aerosol size indicators (effective radius, r_{eff} of submicron and supermicron modes for example) from the spectral information (O'Neill et al., 2003). Lidars (Carswell, 1983), based on the time difference between the emitted and backscattered laser pulses, supply vertical profiles of aerosol and cloud extinction and backscattering coefficient. Lidars also provide an indication of particle size from spectral channels and particle shape via the depolarization channels. The combined use of sunphotometers and lidar, accompanied by supplementary backward trajectories, satellite and other data, has been successfully applied to characterize Arctic aerosol events during the summer time: O'Neill et al. (2008, 2012); Hoffmann et al. (2010); Saha et al. (2010); Stock et al. (2012).

The occurrence and characteristics of aerosols during the Polar Winter, however, are studied to a much lesser extent. The radiation budget during this period is determined by longwave fluxes which results in surface cooling and strong temperature inversions (Bradley et al., 1992). The end result is a very stable lower troposphere that hinders ver-

AMTD
8, 2013–2065, 2015

Synchronous starphotometry and lidar measurements at Eureka

K. Baibakov et al.

tical heat and moisture transfer. It also reduces the aerosol deposition rate (e.g. Quinn et al., 2007). The Polar Winter is also associated with cloudless ice crystal precipitation, commonly termed "diamond dust". Contrary to initial conclusions (Curry et al., 1990), later studies suggest that diamond dust exhibits a negligible radiative effect (Intrieri and Shupe, 2004). However, reports on diamond dust occurrence and microphysical properties in the Arctic are very scarce. Furthermore, surrounding topography can have an important impact on the production of ice crystals. At Eureka station, in the High Canadian Arctic, ice crystals are reported frequently during the winter period. Lesins et al., 2009 show that at least some of these ice crystals are due to the advection of snow from nearby ridges. Crystals formed in this fashion will exert a different radiative influence compared to classical diamond dust. A better characterization of Polar Winter atmospheric phenomena and aerosols in particular represents an important step towards a more comprehensive year-round view of Arctic processes.

One of the principal shortcomings of aerosol studies during the Polar Winter is the absence of AOD measurements. Starphotometry and moonphotometry, based respectively on the radiation from bright stars and Moon, have consequently emerged as possible solutions to the problem. Recent studies show the potential of moonphotometry measurements using sunphotometer-type instruments (Berkoff et al., 2011; Barreto et al., 2012). Despite inherent problems such as changing lunar brightness, moonphotometry can currently provide AODs near full moon (Berkoff et al., 2011). The lunar cycle, however, limits the number of observations down to 30–40 % compared to solar measurements. Leiterer et al. (1995) introduced starphotometry techniques based on extinction of bright-star radiation as a means of generating consistent and regular night-time AOD measurements. Herber et al. (2002) successfully used a combination of sun- and starphotometry to study multi-year AOD dynamics at Ny Ålesund in the High Arctic. This work was based on daily AOD averages and did not focus on individual events or process-level sub-diurnal variations. Furthermore, no coincident lidar data was available for the study period. Alados-Arboledas et al. (2011) showed the feasibility of combining starphotometry and lidar data to study fresh biomass burning

AMTD
8, 2013–2065, 2015

at mid-latitudes. No similar studies of simultaneously operating starphotometers and lidars in the Arctic during the Polar Winter are currently available.

In 2011 an SPSTAR starphotometer joined a Raman lidar as a part of the extensive instrumental suite for atmospheric measurements at the PEARL (Polar Environment Atmospheric Research Laboratory, 610 m altitude) station in the High Canadian Arctic (80° N, 86° W). During the spring of 2011 and 2012 both instruments were operated in tandem in order to study optical properties of aerosols and thin clouds. The purpose of the current paper is to show the capabilities of starphotometer-lidar synergy in the Arctic as a tool for characterizing Polar Winter phenomena in terms of their optical properties. While both instruments are discussed, the focus of the work is on starphotometry with additional details on lidar analysis given elsewhere. We present a process-level analysis of several events that were detected and studied using the combination of the two instruments. This event-based approach is essential to understanding the physics of underlying processes and should precede any statistical or climatological analysis. The results obtained are also important for validating CALIOP space-borne lidar observations acquired during the Polar winter and, alternatively, for giving a spatial context to ground-based lidar and starphotometer observations. The paper is structured as following: Sect. 2 presents the description of the PEARL measurement site, Sect. 3 gives a brief technical overview of instrumentation, Sect. 4 contains important information on data processing and error analysis while Sect. 5 describes principal results obtained within the context of the current work. Finally, Sect. 6 serves as a summary with a review of the main findings.

2 Measurement site

PEARL is a CANDAC (CAnadian Network for the Detection of Atmospheric Change) research site collocated with the Eureka meteorological station in the High Canadian Arctic. It is located on Ellesmere Island, the northernmost island in the Canadian Arctic Archipelago. An overview of climate statistics at Eureka is given in Lesins et al. (2010).

AMTD
8, 2013–2065, 2015

In particular, the average temperature during the coldest months January–March is −37 °C (idem). Strong surface-based temperature inversions are a consistent feature of the Eureka atmosphere. The average inversion temperature (the maximum temperature in the troposphere) is −23 °C while the average values of the inversion thickness and inversion lapse rate are 1200 m and 14 °C km^{-1}, respectively (idem). The winters are extremely dry with the average precipitable water vapor column of less than 2 mm (idem). The surface air is very close to ice saturation during the winter, which explains the persistent presence of the ice crystals occurring at about 50 % of the time (Lesins et al., 2010; Steinbring et al., 2012). The CANDAC scientific equipment found at PEARL includes an array of atmospheric instruments for remotely probing the atmosphere from 0 to 100 km altitude. The optical suite for the measurement of aerosol properties includes an SPSTAR starphotometer, a CRL (CANDAC Rayleigh-Mie-Raman) lidar, and a CIMEL CE-318 sunphotometer.

3 Instrumentation

3.1 Starphotometer

The SPSTAR starphotometer, developed by Dr. Schulz and Partner GmbH acquires measurements of spectral star signals in 17 bands: 419.9, 450.2, 469.2, 500.2, 531.7, 549.8, 605.4, 639.7, 676.1, 750.7, 778.9, 862.3, 933.5, 943.2, 952.8, 1026.0 and 1040.7 nm. The principal components of the SPSTAR are depicted in Fig. 1. These include a Celestrone C11 telescope (aperture/focal length 280 mm/2800 mm), a Baader AZ2000 altazimuth mount (Baader Planetarium GmbH, 2007), a viewfinder, two CCD cameras for centering a star's image on the measuring diaphragm and finally a measuring unit containing a grating spectrometer, a CCD detector and other secondary optics. The FOV of the starphotometer is approximately 0.3°.

AMTD
8, 2013–2065, 2015

3.2 CRL lidar

The CANDAC Rayleigh-Mie-Raman Lidar (CRL) measures elastic and Raman (vibrational and rotational transitions) backscatter at eight different wavelengths and polarizations using transmitted wavelengths of 532 and 355 nm with two pulsed Nd:YAG lasers. The scattered radiation from the eight detectors can be used to determine vertical profiles of aerosol backscatter and extinction, depolarization, temperature, and water vapour (Nott et al., 2012). We note that the physical separation between the lidar and the starphotometer was approximately 40 m.

4 Data processing

4.1 Starphotometry data processing

4.1.1 Calculation of star magnitudes

Starphotometry, like astronomy, uses logarithms of the measured star flux signal to compute star magnitudes. If CN is the number of counts for a particular star measured by starphotometer, the associated star magnitude M is defined as:

$$M = -2.5 \times \log_{10}\mathrm{CN} \quad (1)$$

In reality, starphotometer takes a series of brightness measurements (usually 5) of both a star and background immediately in the vicinity of the star. The CN value used in calculating the star magnitude (Eq. 1) is the difference between the mean star count (SC) and background count (HC):

$$\mathrm{CN} = \mathrm{SC} - \mathrm{HC}. \quad (2)$$

AMTD
8, 2013–2065, 2015

4.1.2 Measurement principle

The diminution of solar light passing through the atmosphere can be expressed via the Beer–Lambert's law (Shaw et al., 1973):

$$I(z) = I_0 e^{-m\tau(z)} \quad (3)$$

where $I(z)$ – solar irradiance as measured on the ground, I_0 – extraterrestrial solar irradiance, m – air mass (e.g. Thomason et al., 1983) and τ – total optical depth. In this work the term "air mass" refers to the optical air mass rather than synoptic air mass.

The value of τ can be decomposed as follows:

$$\tau = \tau_{\mathrm{ray}} + \tau_{\mathrm{aer}} + \tau_{\mathrm{O_3}} + \tau_{\mathrm{NO_2}} + \tau_{\mathrm{H_2O}} \quad (4)$$

where τ_{ray} is the optical depth of molecular scattering (Rayleigh scattering), τ_{aer} is the optical depth due to aerosols (AOD) and $\tau_{\mathrm{O_3}}, \tau_{\mathrm{H_2O}}, \tau_{\mathrm{NO_2}}$ are the optical depths due to absorption by ozone, water vapor, and nitrogen dioxide respectively.

In starphotometry, the Beer–Lambert's takes a form of Eq. (5) with irradiance values converted into magnitudes (Leiterer et al., 1995):

$$M = M_0 + 1.086\tau m \quad (5)$$

where M – measured magnitude on the ground, M_0 – extra-terrestrial instrumental magnitude. The factor ≈ 1.086 in Eq. (5) comes from the product $2.5\log_{10}e$. Two measurement methods are currently used in starphotometry: a two-star method (TSM) and a one-star method (OSM) which is an analogue to classical sunphotometry.

4.1.3 Two-Star Method (TSM)

The two-star method is a relative approach that does not require calibration values. Rewriting Eq. (5) for each of the two stars, subtracting one from another and rearrang-

AMTD
8, 2013–2065, 2015

ing yields (after Leiterer et al., 1995):

$$\tau = \frac{1}{1.086} \frac{(M_1 - M_2) - (M_{01} - M_{02})}{m_1 - m_2} \tag{6}$$

The indices refer to the two stars (also termed "low" and "high" stars referring to their relative elevation) in the same part of the sky that have a sufficient air mass difference ($\Delta m \geq 1$, where $\Delta m = m_1 - m_2$). Assuming that the magnitude difference is the same irrespective of the measurement instrument $M_{01} - M_{02} = M^*_{01} - M^*_{02}$, where M^*_0 refers to the extratterristrial magnitudes taken from the astronomical catalogue of Alekseeva et al., 1996. Equation (6) can then be rewritten in the following form:

$$\tau = \frac{1}{1.086} \frac{(M_1 - M_2) - (M^*_{01} - M^*_{02})}{m_1 - m_2} \tag{7}$$

The starphotometer constantly alternates between the two stars, providing AOD values every 5–6 min depending on the length of the star centering procedure. TSM can be prone to significant point-to-point variations if the atmosphere is not homogeneous (Baibakov, 2009).

4.1.4 One-Star Method (OSM)

Given a value of M_0 (see calibration section below), one can calculate the optical depth, τ, for one star:

$$\tau = \frac{M - M_0}{1.086\,\mathrm{m}} \tag{8}$$

The OSM temporal resolution is 2–3 min. This method is also operationally simpler than the TSM, as only one star needs to be continually followed. The accuracy of the extra-terrestrial magnitudes for all wavelength channels ultimately determines the accuracy of the OSM AODs.

4.1.5 Spectral Deconvolution Algorithm (SDA) processing

The starphotometer AOD spectra were transformed into estimates of fine and coarse mode optical depth at a reference wavelength of 500 nm via the spectral deconvolution algorithm (SDA). This method was employed by O'Neill et al. (2008) and Saha et al. (2010) to analyze co-located sunphotometer and lidar data at Eureka and other Arctic stations. Its basic premise, that aerosol (and cloud) optics are largely driven by independent fine and coarse mode particle size distributions, permits a more fundamental understanding of both optical depths, lidar backscatter profiles and the link between the two.

4.1.6 Cloud screening of the starphotometer data

Photometry data needs to be routinely cloud screened to yield aerosol trends. Smirnov et al., 2000 describe an algorithm based on temporal AOD variations used in the AERONET global sunphotometry network. Similarly, Pérez-Ramírez et al. (2012) apply temporal cloud screening procedures (such as a moving average test) to starphotometry datasets. While this latter algorithm provides a consistent method to remove cloud-contaminated points, the approach and the necessary thresholds should be adapted based on the dataset (D. Pérez-Ramírez, personal communication, 2012). We expect, for example, that Arctic aerosol phenomena will be weaker in magnitude than those at mid-latitudes.

The filters employed in this work are described in Table 2 and partially mimic the methodology proposed by Smirnov et al. (2000) and Pérez-Ramírez et al. (2012). For the range condition, we have eliminated all negative AOD values as well as AODs higher than 0.35. The threshold of 0.35 was chosen as an upper Arctic-AOD bound based on the statistics of Herber et al. (2002) and Tomasi et al. (2007). Clouds are significantly more variable in time than aerosols: hence one of the main cloud filtering tests is an AOD temporal derivative. Smirnov et al., 2000 defined a “triplet stability criterion” that employs three measurements taken 30 s apart over a total of a 1 min period. For a cloud-free atmosphere, the difference between the maximum and the minimum AODs should not exceed 0.02, i.e. $(\tau_{max} - \tau_{min}) < 0.02$. However, there is no analogue to a triplet sampling rate of 30 s^{-1} for the Eureka starphotometer: measurements can only be acquired at a sampling rate of 3 to 10 min^{-1}. Instead, Pérez-Ramírez et al. (2012) used an absolute difference of 0.03 between two consecutive AOD values (obtained, on average, every 5 min) as a filtering condition, which essentially amounts to a rejection criterion of $|d\tau/dt| > 0.006\,min^{-1}$. This criterion turned out to be effective for many cloud scenes (except, of course, for temporally/spatially homogeneous clouds). The moving slope (which is effectively a time derivative computed from an hour-long regression about each optical depth measurement), and the pair-wise time derivative filters are similar and perform comparably, but the former is also sensitive to homogeneous clouds of moderate duration (1 to 1.5 h duration). The pair-wise temporal derivative would not, on average, be sensitive to such variations since its decision protocol is limited to the (usually shorter) temporal range between any two measurements. We found that the empirically chosen 1 h period for the moving slope filter as well as the choice of 0.001 min^{-1} for the slope threshold performed well for the starphotometry datasets. The moving slope threshold of 0.001 min^{-1} is considerably less than the 0.006 min^{-1} threshold employed for the pair-wise time derivative: this is meant to make up for the loss of high frequency sensitivity brought about by the regression over an hour). Additionally, one hour optical depth difference filtering is used by Pérez-Ramírez et al. (2012) to avoid the inclusion of any outliers (while we depend on an AERONET type of (nightly) outlier filter defined in Table 4).

Finally, the outliers filter of Table 2 is also a standard cloud-screening test: one presumes that outliers are very likely to be clouds because of the high frequency variations associated with the latter. We have adjusted the threshold from 3σ of Smirnov et al. (2000) and Pérez-Ramírez et al. (2012) down to 2.5σ given the observed variations in AOD.

It is expected that each filtering condition will have its own drawbacks. For example, the outliers filter will be dependent on the fraction of the cloud-free points in the time series, i.e. if the mean AOD value is too high, some cloud-contaminated values will be left in. When applied consecutively, however, we have found that most of the high-frequency variations associated with what we interpret as cloud features are removed.

Temporal cloud screening, nevertheless, can not eliminate homogeneous clouds with small point-to-point variations, nor can it avoid eliminating highly variable aerosol events such as the incursion of a strong (fine mode) smoke plume (O'Neill et al., 2003). A way to check the performance of the cloud filtering is to use the available spectral information to distinguish between clouds and aerosols (ibid). In fact, the coarse mode of the SDA is in most Arctic cases associated with large super-micron cloud particles.[1] If aerosol optics are dominated by fine mode aerosols (as they are in the Arctic) then the application of the method results in a de facto cloud screening algorithm whose output can be compared (or combined) with a temporal cloud screening algorithm. Quantitatively, one can evaluate the root-mean square difference, $\delta_{\mathrm{flt,RMS}}$, between the fine-mode AOD, τ_{f} and the temporally cloud-filtered AOD, τ_{flt}:

$$\delta_{\mathrm{flt,RMS}} = \sqrt{\frac{1}{N}\sum(\tau_{\mathrm{f}} - \tau_{\mathrm{flt}})^2} \tag{9}$$

where N is the total number of points in a time series.

We also compared the performance of the cloud filtering procedure with the lidar vertical profiles. In many cases, clouds tend to greatly enhance (and sometimes saturate) the lidar backscatter return. Evaluating the vertically integrated lidar signal (lidar optical depth) relative to the τ_{flt} (while being able to visually confirm the presence of cloud from its typically unique appearance as a high frequency, high intensity perturbation in the backscatter coefficient profile) is thus a natural way to ensure the quality of cloud screening.

[1]The course mode can also be associated with large-size aerosols, such as desert dust, volcanic ash and marine salt. However such events are, in our experience, relatively rare at Eureka and/or seasonally constrained.

AMTD
8, 2013–2065, 2015

4.2 Starphotometry calibration

A more detailed treatment of starphotometer calibration is left to Ivanescu et al. (2015). Here we present only a brief discussion.

Despite the obvious advantage of the TSM not requiring a starphotometer calibration, the OSM is considered to be the main operational method. The OSM does not necessitate atmospheric homogeneity and has a higher sampling rate. Furthermore, (A. Gröschke, unpublished data) argues that the accuracy and error analysis is not straight forward for the TSM, given its differential nature.

In order to make measurements with the OSM or extract individual AODs related to the low and high stars of the TSM, one needs to derive extraterrestrial star magnitudes, i.e. magnitudes that a starphotometer would measure outside of the atmosphere (M_0 in Eq. 8). This can be done either by using Langley-type procedures (Shaw et al., 1973) or by calculations from the TSM data. Langley calibration in the Arctic, however, is problematic as it takes many hours for some of the measurement stars to go through a sufficient optical air mass change (Herber et al., 2002). This results in variable measurement conditions and, correspondingly, calibration inaccuracies. Consequently, calibration using a priori acquired TSM data is the de facto calibration method in the Arctic.

Extra-terrestrial star magnitudes can be calculated from TSM data using Eq. (5). Theoretically, only one TSM point is needed to derive M_0 for a particular star. In practice however, one has to analyze at least several nights of measurements, and preferably the entire dataset, to ensure the consistency and stability of the calibration values (A. Gröschke, unpublished data). The problem with Eq. (5) is that the analysis has to be made separately for each measurement star, which is a lengthy and tedious procedure. One solution is to use a procedure akin to the "calibration transfer" proposed by Pérez-Ramírez et al. (2008a) in which several additional stars are also measured during the calibration process (either Langley or TSM). M_0 for those stars can then be easily calculated using Eq. (5) by assuming the value of τ obtained during the calibration procedure.

AMTD
8, 2013–2065, 2015

We employed the star catalogue transfer function or calibration constant, C, to consolidate the ensemble of our multi-star measurements for calibration purposes (Ivanescu et al., 2015). C is defined as:

$$C = M_0^* - M_0 \tag{10}$$

In theory, this allows every TSM measurement to be used to derive calibration values common to all stars. In practice, however, some potential calibration values need to be removed because of the inherent variability in the TSM data (due for example, to contamination by clouds, ice deposition on the optics and instrumental temperature variability). In this work, we imposed the following conditions for a point to qualify for calibration: (a) the point is not marked as cloud by the cloud screening procedure and (b) the error associated with the measurement (δ_τ), does not exceed a certain threshold. In (b) we used $\delta_\tau \leq 0.005$ (significantly less than the accuracy expected for normal field measurements) as a conservative threshold for ensuring good calibration conditions. The resulting calibration values were chosen as averages of the points satisfying all the criteria. The mean standard deviation in relative calibration values (magnitudes) for the bands in the range 420–862 nm was 0.027 corresponding to an AOD error of 0.025.

4.3 Estimation of AOD errors and uncertainties in starphotometry measurements

4.3.1 Sources of calibration, measurement and processing errors

A variety of internal (related to the photometer itself) and external (related to the environment and pointing accuracy) factors can results in starphotometer measurement errors and inconsistencies. Most of the instrumental issues, such as detector linearity and temperature sensitivity as well as dark current, are discussed in detail in Pérez-Ramírez et al. (2008a, b) and A. Gröschke (unpublished data). Starphotometry AOD errors, nevertheless, can have many other sources. For example, TSM measurements are sensitive to the horizontal homogeneity of the atmosphere while the accuracy of the OSM measurements is directly dependent on the quality of the calibration values. Furthermore, the AOD retrieved from some of the SPSTAR visible bands can suffer from insufficiently accurate ozone (and possibly NO_2) correction, while the infrared channels can be affected by water vapor absorption.

Setting aside the cases of the water-vapour sensitive NIR channels (which we did not employ in this work) the most important gaseous absorber in the visible spectra region is ozone. Using an estimated ozone uncertainty of 31 DU (standard deviation from Eureka ozonesonde data) will result in a corresponding standard deviation ($\delta_{\tau,\text{ozone}}$) of 0.004 at 605 nm and 0.001 at 500 nm (assuming a random distribution in ozone concentration). This is substantially less than the nominal starphotometry calibration error of $\delta_{\tau,\text{cal}} = 0.01$ but is not insignificant.

The value of NO_2 optical depth that we employed for our NO_2 corrections was $\tau_{NO_2} = 0.003$. Measurements over Eureka during the late Polar winter of 2004 showed NO_2 columnar abundances between approximately 1.0 and 2.0×10^{15} molecules cm^{-2} (Kerzenmacher, 2005). This yields a range of τ_{NO_2} between approximately 0.0005 and 0.001 for a nominal absorption cross section of 5×10^{-19} cm^2 applied to wavelength channels from the UV to the blue-green portion of the spectrum (O'Neill, 1999). A conservative estimate of 100 % for the relative NO_2 optical depth error (i.e. an absolute error of 0.003) will encompass the late winter Eureka-based estimates of τ_{NO_2}.

The estimated error in the Rayleigh optical depth as given by Frohlich and Shaw (1980) is 0.001 % for the wavelength range of 300 to 900 nm: this yields a maximum Rayleigh optical depth error of 0.00043 at 380 nm. While this may be a bit optimistic for the Arctic it is most likely of the correct order of magnitude and therefore negligible compared to O_3 and NO_2 errors. Rayleigh optical depths are also pressure corrected: we roughly estimate the uncertainty associated with the pressure correction to be ~ Frohlich and Shaw's 0.001 % relative error (~ 1 hPa over 1013 hPa).

Some of the other factors that might effect AOD measurements include imprecision in star pointing and tracking (resulting in either underestimated star signal or overcompensated background correction), vibrations due to winds ($> 8\,\mathrm{m\,s^{-1}}$), light pollution due to Moon or artificial lightning and ice deposition on the telescope. A detailed description of these issues will be found in Ivanescu et al. (2015).

4.3.2 Estimated total error in τ_{aer}

From Eq. (4) the total AOD error, $\delta_{\tau_{\mathrm{aer}}}$, is a function of the errors in all the component parameters employed in its retrieval. Expressing Eq. (3) in terms of numerical counts, CN and CN_0, $\delta_{\tau_{\mathrm{aer}}}$ can be estimated as following (see Appendix A for details):

$$\delta(\tau_{\mathrm{aer}}) = \sqrt{\left(\frac{1}{m}\right)^2 \left\{ \left(\frac{\delta(\mathrm{CN}_0)}{\langle \mathrm{CN}_0 \rangle}\right)^2 + \left(\frac{\delta(\mathrm{CN})}{\langle \mathrm{CN} \rangle}\right)^2 \right\} + \delta^2(\tau_{\mathrm{O_3}}) + \delta^2(\tau_{\mathrm{NO_2}}) + \delta^2(\tau_{\mathrm{H_2O}})} \quad (11)$$

where $\frac{\delta(\mathrm{CN}_0)}{\langle \mathrm{CN}_0 \rangle}$ is the calibration error, $\frac{\delta(\mathrm{CN})}{\langle \mathrm{CN} \rangle}$ the measurement error, $\langle \mathrm{CN}_0 \rangle$ and $\langle \mathrm{CN} \rangle$ are the average values of CN and CN_0 and $\delta(\tau_{\mathrm{O_3}}), \delta(\tau_{\mathrm{NO_2}}), \delta(\tau_{\mathrm{H_2O}})$ the errors associated with the estimation of ozone, NO_2 and H_2O optical depths respectively. This yields an OSM error estimate of $\delta(\tau_{\mathrm{aer}}) = 0.03$ for a typical air mass value of $m = 1$.

4.3.3 AOD error due to incomplete cloud screening

The estimate of $\delta_{\tau_{\mathrm{aer}}}$ above is for the list of error contributions that are readily quantified with some coarse degree of accuracy (or they can be highly inaccurate but very small). It precludes "catastrophic errors" such as significant ice condensation on the optics or serious tracking errors in the star measurement or in the background measurement modes. The oftentimes inadequate nature of temporal cloud screening remains an error source which is highly variable. If we anticipate the results of our spectral vs. temporal cloud screening comparison (Sect. 5.5) in the presence of (spatially inhomogeneous) clouds whose presence is readily filtered out (Fig. 9) then we can at least get out an order of magnitude error associated with the shortcomings of temporal cloud screening in the presence of optically thin clouds. Based on the RMS computations for the

AMTD
8, 2013–2065, 2015

illustrative case of Fig. 9 we obtain $\delta(\tau_{\text{aer, post-cloud-screening}}) \lesssim 0.03$, a number which will be inflated by, for example, inaccuracies in the retrieval of τ_f and the possible presence of thin homogeneous cloud that escapes temporal cloud screening. This is an attempt to describe a worst case scenario: in the absence of competitive coarse mode signal, $\delta(\tau_{\text{aer, post-cloud-screening}})$ will be significantly smaller.

4.4 CRL processing

The lidar return contains information about the atmosphere in terms of the backscatter and extinction coefficients, $\beta(z)$ and $\kappa(z)$. The former describes how much light is scattered into the backward direction and determines the strength of the return lidar signal from the sampling volume at altitude z. The extinction coefficient describes the combined capacity of all particles, to diminish the laser beam intensity in the sampling volume at altitude z. The profile of the extinction coefficient between the receiver and the sampling volume acts to attenuate the outgoing and return signal from the sampling volume at altitude z. Assuming that the light is scattered mostly by air molecules (index "m") and aerosols (index "a"), $\beta(z)$ can be expressed as:

$$\beta(z) = \beta_m(z) + \beta_a(z) \tag{12}$$

One distinguishes between elastic (Rayleigh) and inelastic (Raman) scattering. In the former case, the frequency of the scattered photon is the same as the frequency of the incident photon. Raman scattering (which a Raman lidar such as CRL makes use of) changes the internal energy state of specific types of molecules in the path of the beam. The resulting frequency shift of the scattered photon can be used to separate molecules from aerosols as the latter undergo only elastic scattering.

There are two techniques used for the purpose of determining the aerosol backscatter coefficient for the CRL. The first is the Klett inversion (Klett, 1981), which is applied to the elastic scattering channel at 532 nm. The second technique, the Ratio technique (Ansmann and Müller, 2005), uses the elastic scattering channel (532 nm) and a Nitrogen Raman scattering channel (607 nm) to obtain profiles of backscatter coefficient.

AMTD
8, 2013–2065, 2015

The Klett inversion requires an estimation of the aerosol extinction to backscatter ratio (or lidar ratio, S_a), which can be difficult to estimate. The Ratio technique however is much noisier due to the low scattering cross section of Raman scattered radiation. Given that the star photometer is an extinction based instrument (its output is optical depth), an estimate of the lidar ratio needs to be applied to both techniques to convert the backscatter coefficient to extinction coefficient and subsequently optical depth (an alternate technique, by Ansmann et al., 1992, which employs the transmission of the Raman channel to directly measure extinction coefficient also suffers from the weak and noisy nature of the Raman channel as well as the fact that a noise-sensitive vertical derivative has to be applied to yield extinction coefficient). A common issue with lidar monitoring is the incomplete overlap region. The overlap region is defined as a region where the field of view of the receiving system does not fully capture the backscatter from the transmitted radiation. This will occur for a range of altitudes near the surface. By using both aerosol techniques mentioned above, a correction can be applied to the Klett inversion as shown by Wandinger and Ansmann, 2002. The Ratio technique should not suffer from overlap effects due to the two detectors (that measure the elastic and inelastic signals being ratioed) theoretically having the same incomplete overlap region (idem). In reality, however, this is not the case and a correction is applied to the Ratio technique analysis by using "clear–sky" measurements (minimal aerosol and cloud) from which the profile of aerosol backscatter would be weak. Applying these overlap corrections allows the CRL to measure down to approximately 200 m for both techniques.

4.5 Lidar Optical Depth computations

4.5.1 Simple threshold approach for aerosol/cloud discrimination

As a part of the analysis, we integrated the lidar profiles to calculate lidar fine, coarse mode and total optical depths (we adopted the notation whereby primed optical depths, τ_f', τ_c', $\tau_a' = \tau_f' + \tau_c'$ are derived from lidar profiles whereas unprimed optical depths, τ_f,

τ_c and $\tau_a = \tau_f + \tau_c$ are derived from the starphotometry data). To do this we had to assume lidar ratios based on the following binary fine/coarse classification scheme. Features with backscatter coefficient values higher than a specific threshold (β_{thr}) were considered clouds or ice crystals and assigned to a cloud/ice crystal class while all other backscatter coefficient samples were classified as fine mode aerosols (implicit in this latter assignment is the assumption that aerosol optical activity is dominated by fine mode aerosols). Cloud/ice crystal samples were assigned a lidar ratio value of $S_c = 20$ sr. This value is a typical cloud lidar ratio: it is, for example, contained within the 19–25 sr range defined in the CALIPSO data processing algorithm (ASDC, 2013). All non-cloud layers were assigned a value of $S_f = 71$ sr (corresponding to the CALIOP class "urban/industrial pollution", idem, and, for example, a value that is not far from the value of 59 sr employed by O'Neill et al. (2012) for volcanic sulfates over Eureka). While aerosols exhibit a fairly large natural variation in S_f, the chosen value was found to perform well for most scenes observed at Eureka.

4.5.2 Sensitivity study

To select a proper value of β_{thr} that does not produce a significant bias in favor of either clouds or aerosols, we performed a sensitivity study for all events that were investigated in this study: 21 February 2011, 9 and 10 March 2011 and 13–15 March 2012 (the detailed discussion of these events is presented in Sect. 5). We varied β_{thr} from $1 \times 10^{-10}\,\mathrm{m^{-1}\,sr^{-1}}$ (all/most features classified as clouds) to $1 \times 10^{-3}\,\mathrm{m^{-1}\,sr^{-1}}$ (all/most features classified as aerosols) and studied the variation of $\langle\tau'_x\rangle$–$\langle\tau_x\rangle$ and R^2_x (where the angle brackets "$\langle\rangle$ " indicate an average, the subscript x = f, c or a, R^2_x is the coefficient of determination and where the averages and the R^2_x values were evaluated across the duration of the measuring period). Our sensitivity study was focused more on fine mode aerosols (which, as discussed above, generally means aerosols in the absence of any significant presence of coarse mode aerosols) since this is our principle area of

AMTD
8, 2013–2065, 2015

interest and since fine mode aerosol variation is generally more subtle and difficult to detect in the Arctic.

Illustration using the 9 March case study

Figure 2a and b illustrate the results of the sensitivity study for 9 March 2011. The top plot of Fig. 2b shows the fixed starphotometer optical depth means ($\langle\tau_f\rangle$, $\langle\tau_c\rangle$ and $\langle\tau_a\rangle$ averages taken across the 9 March measuring period) and the computed values of $\langle\tau_f'\rangle\langle\tau_c'\rangle$ and $\langle\tau_a'\rangle$ varying as a function of β_{thr} while the middle plot shows the difference between these means ($\langle\tau_f\rangle$ and $\langle\tau_c\rangle$ are practically superimposed; the relatively large value of $\langle\tau_c\rangle$, as discussed in Sect. 5.1, was due to thin-cloud contamination). As expected $\langle\tau_f'\rangle \rightarrow 0$ when β_{thr} is very small and the classification algorithm declares all particles to be clouds while $\langle\tau_c'\rangle \rightarrow 0$ when β_{thr} is very large and the classification algorithm declares all particles to be fine mode aerosols.

The bottom graph of Fig. 2b shows the different components of $R_x^2(\tau_f'$ vs. $\tau_f)$ varying as a function of β_{thr}. One can observe the promising result that both the β_{thr} ($\langle\tau_f'\rangle - \langle\tau_f\rangle = 0$) zero crossing (red dotted vertical line of Fig. 2) and $\beta_{thr}(R^2_{f,\,peak})$ are of the same order of magnitude while noting the more disconcerting result that the rapid variation of R_f^2 implies that the difference is a compromising problem. However, as discussed in the next section, we can play upon the relatively large uncertainties in the starphotometer and lidar optical depths to define a large zero crossing region which encompasses the peak in R_f^2.

Figure 2a provides insight into the detailed behavior of two critical values of β_{thr}: a value of $2\times10^{-7}\,m^{-1}\,sr^{-1}$ which corresponds to a near zero value of R_f^2 and a value of $4\times10^{-7}\,m^{-1}\,sr^{-1}$ which corresponds approximately to $\beta_{thr}(R^2_{f,\,peak})$. The top pane contains total, fine and coarse mode AODs from the SDA at 500 nm (τ_a, τ_f and τ_c respectively) and the lidar AODs at 532 nm (τ_a', τ_f' and τ_c' respectively), while pane 2 shows lidar backscatter cross-section profiles at 532 nm. Values of τ_f' and τ_c' were

AMTD
8, 2013–2065, 2015

calculated in accordance with Sect. 4.1.5 where the binary lidar ratio assignments are determined from the aerosol/cloud classification of pane 3.

If one compares the τ_f' variation of Fig. 2a with the backscatter profiles and, in particular, the classification panes, it is clear that the increase in τ_f' from left pane 1 to right pane 1 is due to the "gain" of aerosols in the plume located at around 5 km (also keep in mind that the τ_f component of the comparison is fixed). This plume (which we hypothesize, from experience, to actually be of aerosol nature) is responsible for the right to left increase in τ_f' (from the left hand pane 1 to the right hand pane 1) and the greater thickness of the plume in the latter part of the day is responsible for the proportionate (right hand pane 1) increase in τ_f' over that period (compared to the quasi constant value of τ_f' in the left hand pane). This increase across the measurement period is sufficient to augment R_f^2 from a negligible value of 0.02 to a significant value of 0.62 (more details are given in Sect. 5.1). It is our contention that the most robust arbiter of physical truth is arguably R_x^2 (and R_f^2 in the particular case of fine mode aerosols) because it can show a correlation of independent optical data and because it is less dependent on calibration and algorithmic artifacts. The $\langle\tau_f'\rangle$–$\langle\tau_f\rangle$ differences of Fig. 2b are more readily swayed by the relatively large absolute uncertainties in τ_f due to calibration and algorithmic shortcomings as well as the uncertainties in τ_f' due to problems associated with the assigned value of S_f as well as the lidar calibration procedure.

Some comments also need to be added concerning the general behavior of the R_x^2 curves in Fig. 2b. R_c^2 remains moderately large and nearly constant and then drops off for $\beta_{trh} >\sim 1\times10^{-6}$. This reflects the fact that the backscatter coefficients of what we believe to be clouds between 7 and 10 km stand out quite distinctly until their rather large threshold value is surpassed and all samples are declared to be fine mode aerosols. Beyond this point the values of R_a^2 remain moderately large and constant. Since all backscatter samples have, at this point, been declared to be fine mode aerosols, the clouds between 7 and 10 km take on the artificial condition of $\tau_f' \rightarrow \tau_a'$ (accompanied by excessively large values of τ_f' and τ_a' due to the large value of S_f = 71 sr being artificially ascribed to clouds). Since τ_a variation is, in general, dominated by τ_c variation (cf. the

AMTD
8, 2013–2065, 2015

top panes of Fig. 2a) then it is not surprising that the "cloud dominated" variation of τ'_a at artificially large values of β_{thr} is moderately well correlated with τ_a. It can also be observed in Fig. 2b that this case of artificially large τ'_a ($\cong \tau'_f$) is characterized by R^2_a values that are identical to R^2_a values when β_{thr} is very small: the only differences between the two artificial cases of ostensibly pure fine and coarse mode cases are the two different values of lidar ratio (and so the correlation with τ_a is identical).

Ranges of optically acceptable β_{thr}

Figure 3a shows a conceptual representation of β_{thr} uncertainty as a function of a presumed uncertainty in the differences of the means for each of the three components. In the application of this concept to $\langle\tau'_x\rangle$–$\langle\tau_x\rangle$ plots such as the middle graph of Fig. 2b, we assumed an error equal to the nominal uncertainty of 0.03 in the starphotometer optical depths as per Sect. 4.3.2 and applied this to all the events investigated as part of this paper to obtain the top graph of Fig. 3b. One can observe that the β_{thr} ranges of $\langle\tau'_f\rangle$–$\langle\tau_f\rangle$ are clustered near the β_{thr} value of $4 \times 10^{-7}\ m^{-1}\ sr^{-1}$ represented by the dashed, grey vertical line. Indeed, for simplicity, we assumed a β_{thr} nominal value of $4 \times 10^{-7}\ m^{-1}\ sr^{-1}$ for all the case studies discussed in Sect. 5 below, unless indicated otherwise (we leave the discussion of the effects of this choice to those case studies). The clustering of the fine mode β_{thr} ranges, along with the 9 March 2011 illustration of the previous section, suggests in a general sense, that τ'_f as well as τ_f can, in spite of the typically stronger variability associated with τ'_c and τ_c, be justifiably associated with the presence of fine mode aerosols in the atmosphere. Those β_{thr} ranges associated with $\langle\tau'_c\rangle$–$\langle\tau_c\rangle$ and $\langle\tau'_a\rangle$–$\langle\tau_a\rangle$ that are large merely reflect a situation where $\langle\tau'_c\rangle$ and $\langle\tau'_a\rangle$ change little with β_{thr} (the cloud/aerosol classification changes little with β_{thr}).

The bottom graph of Fig. 3b shows the uncertainty in β_{thr} given a requirement that R^2_x be greater than 0.19. The threshold of 0.19 was selected in an attempt to broadly quantify a β_{thr} range of significant R^2_x values for all events: it represents a cutoff whose

AMTD
8, 2013–2065, 2015

Synchronous starphotometry and lidar measurements at Eureka

K. Baibakov et al.

probability distribution was significantly different from zero for all events of the study.[2] One can observe that the positions of the R_f^2 ranges are also clustered near the β_{thr} value of 4×10^{-7} m^{-1} sr^{-1}. The notable exceptions to this observation are isolated points of higher R_f^2 values for 14 and 15 March 2012. The former (large β_{thr}) case represents a region where τ_c' is negligible and thus where τ_f' is characterized by R_f^2 values that are strongly influenced by coarse mode variance (when τ_c is not negligible and there is every evidence in the behavior of the backscatter profile that τ_c' is artificially low). In the latter (small β_{thr}) case, τ_f' is negligible at such a small value of β_{thr} and so the correlation with τ_f is optically insignificant (it depends on relatively few, general noisy samples of β). Finally, the reasons for the broad β_{thr} ranges for R_c^2 and R_a^2 have already been discussed in the analysis of the 9 March 2011 illustration above.

5 Event analysis

5.1 Short-term aerosol events (9–10 March 2011)

Figure 4 shows starphotometry and lidar data obtained at Eureka between 00:00 on 9 March and 13:00 on 10 March 2011 all time values in this work refer to UTC. Considerable atmospheric complexity during the given time period is manifested by the presence of what we interpret to be several distinct features: aerosol layers up to 6 km, tropospheric clouds between 6 and 10 km as well as optically weak PSC layers above 14 km. In addition, 10 March is associated with surface-layer ice-crystals in the lowest 500 m (discussed in more detail below). The $\langle\tau_f\rangle$ value of 0.06, across the total period, is generally dominated by the low amplitude backscatter aerosol layers between 1 and 6 km. Aerosol plumes were especially prominent on 9 March, gradually thinning out

[2] More precisely, the lower uncertainty of Fisher's Z transformation ($Z_x = \ln[(1+R_x)/[(1-R_x)]]$) was greater than zero at a 95 % confidence level (Spiegel, 1961).

AMTD
8, 2013–2065, 2015
Synchronous starphotometry and lidar measurements at Eureka
K. Baibakov et al.

towards the end of the 2 day period. We see that, in general, τ_f' agrees marginally well with τ_f (RMS difference of 0.03) with τ_f being generally less than τ_f'.

Focusing on the fine mode variation and shorter term scales during both 9 and 10 March (Fig. 5), the best correlation between τ_f' and τ_f is achieved on 9 March (left side of Fig. 5) with an R_f^2 value of 0.61. On both days, we ignored high frequency AOD variations after approximately 10:25, inasmuch as the measurements beyond that time were influenced by the background scattering signal associated with the rising sun. For 10 March, the degree of correlation between τ_f' and τ_f is marginal at best (R_f^2 value of 0.18), but the temporal variation in both τ_f and τ_f' is weak to begin with. We would argue nonetheless, that both τ_f' and τ_f react (with a precision $\lessapprox$0.01) on both days to the most optically active portion of the (presumed) fine mode layer between a few hundred meters above ground-level to between around 6 km on 9 March to 8 km on 10 March (the most optically active regions being between the dashed purple lines of Fig. 5). It should be pointed that the 10 March R_f^2 vs. β_{thr} curve shows a second, marginally significant peak around $5 \times 10^{-8}\,m^{-1}\,sr^{-1}$ in addition to the peak around $4 \times 10^{-7}\,m^{-1}\,sr^{-1}$ (cf. Fig. 3b). The lower β_{thr} peak represents a β_{thr} region where τ_f' is virtually constant across that time period (virtually all the plume structure seen on Fig. 5 has been assigned to the cloud class) and the resulting τ_f' variation $<\sim 0.003$. This means that any correlation between τ_f' and τ_f is likely influenced, if not dominated by non physical perturbations of τ_f'.

Both examples of Fig. 5 appear to show an appreciable sensitivity to quite small changes in fine mode aerosol optical depth as well as a temporal coherence between passive and active measurements which is rarely if ever reported in the literature. We note that the PSCs at around 14 km (see also Fig. 4 for a more general context) are characterized by optical depths that are significantly less than the tropospheric optical depths and are a minor influence on this analysis.

Returning to Fig. 4, one can observe that τ_c' corresponds moderately well with τ_c, especially for the cloud feature in the first half of 9 March (the RMS difference between τ_c' and τ_c is 0.04 for the whole period, and 0.03 for 9 March). Of particular interest are the three coarse mode peaks on 10 March that are evident in both starphotometry and lidar data. The signal enhancements are due to surface layer ice-crystals and are discussed in more detail in Sect. 5.3.

All of these indicators would tend to confirm our original hypothesis that both τ_f' and τ_c' can be approximately derived from the β_{thr} classification paradigm and that the estimates are approximately coherent with τ_f and τ_c respectively. The lidar errors inherent in such a comparison include the errors associated with the classification criteria, the assigned lidar ratio values ($\approx$ 10–20 sr or hence $<\sim$ 2–40 % error in predicted τ_f' or τ_c' values), and artifacts such as the vertical streaks (banding) observable in pane 2 of Fig. 5 (which we estimate to $<\sim$ 0.01 in those figures) These vertical-streak artifacts are due to a low number of photon counts in the normalization region, which makes it difficult to measure this region accurately. The low number of photon counts is because the normalization region is at a high altitude near the tropopause, which is for the purpose of having minimal aerosol contamination. This error in the normalization region will propagate downward in the lidar profile. The starphotometer errors include the estimated AOD calibration errors ($\approx$ 0.03) and SDA errors ($\approx$ 10 %).

5.2 Multi-night aerosol event (13–15 March 2012)

Figure 6 shows, what we suspect to be a multi-night event (low frequency, τ_f' and τ_f variation across the three nights with mild peaking on 14 March) as well as an illustration of the difficulties one encounters in attempting to identify low frequency and low amplitude fine mode events when there is relatively little temporal variation associated with the fine mode optical depth (which means that it is important to retain as much τ_f' vs. τ_f data as possible on each of the three nights). The mixture of aerosol and cloud on 13 March is particularly fraught with difficulties in that the τ_c' and τ_c signals tend to dominate their fine mode analogues earlier in the night, while the τ_c' vs. τ_c as well as τ_f' vs. τ_f results tend to diverge in the latter part of the night. We found, as part of our β_{thr} sensitivity study (applied to the entire three night period), that the latter part of 13 March was a highly sensitive classification period since classification results changed rapidly

Discussion Paper | Discussion Paper | Discussion Paper | Discussion Paper |

AMTD

8, 2013–2065, 2015

Synchronous starphotometry and lidar measurements at Eureka

K. Baibakov et al.

with small changes in β_{thr} (due to the presence of what was likely a mixture of heterogeneous thin cloud and fine mode aerosols). The result was that our R_f^2 vs. β_{thr} plot showed a sharp maximum similar to the bottom graph of Fig. 2b but where the peak was only marginal (as per the R_f^2 criterion of Fig. 3b) and below the range of acceptable $\langle\tau_f'\rangle$–$\langle\tau_f\rangle$ differences (Fig. 3b). Thus, while the R_f^2 peak suggests that this might well be a multi-night event, the actual $\langle\tau_f'\rangle$–$\langle\tau_f\rangle$ range seems to indicate an inconsistency in our criteria. If one argues in favour of the robustness of the R_f^2 criteria then we would have to appeal to such factors as τ_f retrieval errors or the possibility that a simple binary cloud classification (cloud aerosol/separation) algorithm is, at least in this case, too simplistic.

5.3 Low altitude ice crystals (10 March, 2011)

The proper detection of τ_c, whether it represents coarse mode aerosols or cloud, is an important test of the performance of the SDA (which is strongly dependent on the spectral curvature fidelity of the starphotometer optical depths) and of the performance of any cloud screening algorithm. Figure 7 shows an extract of Fig. 4 for 10 March 2011 with the lidar data in panes 2 and 3 displayed only for the lowest 2 km. The peaks in starphotometry AODs at 03:25, 06:35 and 09:00 have a clear association in time with the obvious increase in backscatter coefficient in the lowest 250 m. Furthermore, the SDA indicates that the observed features are coarse-mode (τ_c) dominant. While some weak backscatter layers are present at the higher altitudes (the relatively strong tropospheric and weaker stratospheric features of pane 2 in Fig. 4),τ_c' is dominated by the low-altitude features. For the most extreme vertical profiles between 06:00 and 08:00, the first 250 m can contribute more than 80 % to the total integrated value. The positions of the peaks in τ_c' correspond well in time to those of τ_c: the τ_c' values at the τ_c peak times of 03:25 and 09:00, however, are significantly lower than the corresponding τ_c values. At these low altitudes the laser beam is not entirely within the field of view of the detection optics, so it is likely that the inconsistencies between τ_c' and τ_c are, at least in part, related to an incomplete overlap correction. However this correction is a crude approximation whose uncertainty increases with the proximity to the ground. It fails to explain why $\tau_c' > \tau_c$ about the 06:35 peak and one must therefore appeal to additional factors to explain the discrepancy (SDA retrieval errors, errors in cloud/aerosol classification etc) In the case of overlap function problems, starphotometry measurements become particularly relevant given inherent lidar difficulties at the lowest altitudes.

5.4 Mid-tropospheric thin clouds (21 February 2011)

Generally, clouds are relatively opaque and strongly attenuate the inherently weak star radiation. Some types of clouds (such as thin ice clouds, TICs), however, can be optically thin, while extending vertically for several kilometers. An example of such a cloud event was observed on 21 February, 2011 at Eureka is shown in Fig. 8 (some aspects of this event were originally discussed in Ivanescu et al., 2011).

The optical depth values of pane 1 show a significant variation between 0.2 and 0.8 during the 11.5 h measurement period. The SDA applied to the starphotometry dataset shows the dominance of the coarse mode particles which compose the cloud. The assumption that the coarse mode optical depth variation can be ascribed to clouds is supported by the CRL data showing strong backscatter coefficient features in the 3–5 km altitude range. Perhaps more convincingly, the presence of clouds is confirmed by the high depolarization ratio values[3] (up to 40–50 %, pane 4) which are spatially correlated with the high backscatter coefficient values of pane 2. Such high depolarization ratio values are typical of ice crystal clouds. The CRL integrated signal associated with cloud features, τ_c', shows good correlation ($R^2 = 0.78$) with the starphotometry coarse mode, τ_c. τ_c' is nevertheless, somewhat smaller than τ_c beyond 05:00. The difference can, at least in part, be due to the prescribed generic lidar ratio of 20 sr for the clouds. A slightly higher value of $S_a = 25$ sr might be more appropriate as it would result in bet-

[3]Depolarization ratio data for 2011 was generally noisy due to technical difficulties, in this case, however, a strong signal stood out above the noise.

ter agreement between τ_c' and τ_c (we would also note that the overlap function at the relatively high-altitude positions of the clouds is not an issue). The reader will further note that the fine mode optical depth is relatively stable with realistic values in spite of being dominated by the coarse mode contributions. The τ_f values are around 0.07 until 09:00 and agree closely with those of τ_f'. Beyond 09:00 τ_f rises to the mean value of 0.12, but τ_f' does not undergo a similar change. This discrepancy might, for example, be associated with the SDA uncertainties, given the predominantly coarse-mode scene and/or errors in the aerosol/cloud classification scheme employed to retrieve τ_c' (in the latter case, the apparent stability of τ_f' seen in Fig. 8, after around 10:00, could, in actual fact, be a failure of the classification algorithm to respond to an increased presence of fine mode particles).

5.5 Example of cloud screening

We examined the performance of temporal cloud screening on several examples and present one of the more instructive cases in this section. Figure 9 shows the results of filters applied to the AOD time series on the 10 March 2011 low-altitude crystal event of Fig. 7 (filter 1, the optical depth upper limit condition, is not employed in this case as all AODs are smaller than 0.35).

As established in Sect. 5.3, the AOD peaks centered at 03:25, 06:35 and 09:00 are due to surface layer ice crystals in the lowest 500 m. In order to eliminate this non-aerosol contribution we attempt to use the temporal cloud screening algorithm defined in Sect. 4.1.6 (and effectively extend the definition of "cloud" to include these low lying ice crystals). Pane 1 shows points that were classified by the cloud filters as contaminated ("CldScr" series), i.e. points that were associated with abrupt high-frequency temporal variations. For this date, filters performed well in flagging the optical depths associated with the coarse-mode peaks. The remaining points of the black curve (which in principle are associated only with aerosol signal) should be comparable to the fine mode red curve: the RMS difference between the two improved from 0.07 to 0.03 without and with cloud filtering. Given the limited scarcity of the starphotometry dataset,

AMTD
8, 2013–2065, 2015

we leave aside the question of just how much the two should agree to future analyses: one could argue, for example, that the cloud-screened AODs contain a small OD contribution due to coarse mode aerosols and/or homogeneous clouds or one could equally well question the accuracy of the SDA fine mode retrieval which becomes less accurate for small AODs (O'Neill et al., 2003).

6 Summary and conclusions

In this paper, we presented recent progress related to the night-time optical depth retrievals of aerosols and clouds using starphotometry at the high Arctic PEARL station. Optical measurements, and specifically AOD measurements, acquired during the Polar Winter are scarce but nonetheless represent an important source of information for the development of aerosol optical climatologies, instrumental intercomparisons, satellite validation (such as CALIOP) and tie-down points for aerosol/cloud models. In the spring of 2011 and 2012, the SPSTAR starphotometer was operating whenever possible, acquiring AOD measurements in tandem with the acquisition of vertical profiles from the CRL Raman lidar.

Starphotometry is a relatively new technology that is subject to weak-signal problems exacerbated in the extreme Arctic conditions. The accuracy of the derived AODs ultimately depends on the choice of calibration values and other instrumental and environmental factors such as optics degradation or background field characterization. Given the slowly changing optical air mass values characteristic of most measurement stars, Langley calibration is problematic in the Arctic. The SPSTAR was calibrated using differential two-star measurements. Only points satisfying cloud filtering and measurement uncertainty criteria were considered for calibration. The quality of the calibration values (C) was confirmed by studying their evolution throughout the entire measurement period. The AOD errors due to the spread in the potential calibration values were estimated to be 0.025. The total error in AOD, $\delta(\tau_{aer})$, was estimated to be $\delta(\tau_{aer}) \lessapprox 0.03$ (for an optical air mass of 1).

AMTD
8, 2013–2065, 2015

Synchronous starphotometry and lidar measurements at Eureka

K. Baibakov et al.

Short-time scale (≈ minutes) process-level analysis of aerosol and cloud events simultaneously captured in photometric and lidar data is essential to ensure that extracted extensive (bulk) and intensive (per particle) optical and microphysical indicators are coherent and physically consistent. At the same time, this type of analysis is rarely addressed in the literature and we have found no measurement series that deal with process-level analysis of Polar Winter datasets. Using the starphotometry-lidar synergy we have detected and characterized several distinct events throughout the measurement periods. In particular, we provided case studies of: aerosols (short term aerosol events on 9 and 10 March 2011, a potential multi-night aerosol event across three polar nights (13–15 March 2012), ice crystals (10 March 2011) and thin clouds (21 February 2011). For this analysis, we employed prescribed values of extinction to backscatter lidar ratio values and applied these values to a simple threshold based classification of the lidar backscatter images. In general, there was good agreement in terms of the physical coherence between fine and coarse mode starphotometry ODs (τ_f and τ_c) and corresponding lidar optical depths of aerosol and cloud layers (τ_f' and τ_c'). The best correlation between τ_f and τ_f' was achieved for an aerosol event on 9 March with an R^2 (coefficient of determination) value of 0.61, while the measurement during the thin cloud event observed on 21 February 2011 showed the best correlation between τ_c and τ_c' ($R^2 = 0.78$). We also argued that R^2 was the most robust means of comparing lidar and starphotometer data since it was sensitive to significant optico-physical variations associated with these two independent data sources while being minimally dependent on retrieval and calibration artifacts. Differences between τ_f' and τ_f as well as τ_c' and τ_c are clearly also useful but are dependent on such artifacts.

Studying seasonal aerosol trends necessitates cloud-screening procedures. We have developed several tests that help detect cloud-contaminated optical depths based on high-frequency optical depth variations. In addition, we used fine-mode AOD as a means of performing de facto spectral cloud screening and accordingly, as a means of verifying the quality of temporal cloud screening. In general, a combination of temporal filters performs well for most cloud features with cloud-screened optical depths (AOD)

AMTD
8, 2013–2065, 2015

being in good agreement with spectrally cloud-screened optical depths (τ_f). Temporal cloud screening, nevertheless, predictably fails for low-frequency variations associated with ice crystals or homogeneous clouds. In this case, spectral cloud screening has a distinct advantage of not being dependent on temporal variations.

We conclude by saying that the synergism employed in the present work enabled the assemblage of evidence for events whose process-level understanding will inevitably generate greater confidence in starphotometer retrievals as well as starphotometer/lidar comparisons and will lead to the improvement of critical statistics such as multi-year climatologies. Such an assemblage is non trivial in a low AOD (low signal to noise) environment such as the Arctic.

Appendix A: Estimated total error in τ_{aer}

The total AOD error is a function of the errors in all the component parameters employed in its retrieval. Expressing Eq. (3) in terms of numerical counts yields:

$$\mathrm{CN} = \mathrm{CN}_0 e^{-m\tau} \quad \text{(A1)}$$

where CN_0 is the extraterrestrial numerical count value for a given star at a given wavelength. Differentiating this expression yields:

$$\mathrm{dCN} = e^{-m\tau}\mathrm{dCN}_0 + \mathrm{CN}_0(-m\tau)e^{-m\tau} \quad \text{(A2)}$$

$$\frac{\mathrm{dCN}}{\mathrm{CN}} = \frac{\mathrm{dCN}_0}{\mathrm{CN}_0} - m\mathrm{d}\tau \quad \text{(A3)}$$

$$\mathrm{d}\tau = \frac{1}{m}\frac{\mathrm{dCN}_0}{\mathrm{CN}_0} - \frac{1}{m}\frac{\mathrm{dCN}}{\mathrm{CN}} \quad \text{(A4)}$$

Using Eq. (4) we can solve for the total error in the aerosol optical depth:

$$\mathrm{d}\tau_{aer} = \frac{1}{m}\frac{\mathrm{dCN}_0}{\mathrm{CN}_0} - \frac{1}{m}\frac{\mathrm{dCN}}{\mathrm{CN}} - \mathrm{d}\tau_{ray} - \mathrm{d}\tau_{O_3} - \mathrm{d}\tau_{NO_2} - \mathrm{d}\tau_{H_2O} - \mathrm{etc} \quad \text{(A5)}$$

AMTD
8, 2013–2065, 2015

We will, from this point on, assume that Rayleigh optical depths errors are negligible and that H_2O optical depth errors are negligible in the UV and visible spectral regions. Assuming that all remaining errors are randomly distributed, an average over a large number of samples at a given solar air mass will yield the mean square sum;

$$\langle d\tau_{aer} \rangle = \sqrt{\frac{1}{m}\left\langle \left(\frac{dCN_0}{CN_0}\right)^2 \right\rangle + \frac{1}{m}\left\langle \left(\frac{dCN}{CN}\right)^2 \right\rangle + \langle (d\tau_{O_3})^2 \rangle + \langle (d\tau_{NO_2})^2 \rangle} \tag{A6}$$

We then approximate the differentials by their RMS difference relative to their true value and the denominators by their mean to obtain;

$$\delta(\tau_{aer}) = \sqrt{\left(\frac{1}{m}\right)^2 \left\{ \left(\frac{\delta(CN_0)}{\langle CN_0 \rangle}\right)^2 + \left(\frac{\delta(CN)}{\langle CN \rangle}\right)^2 \right\} + \delta^2(\tau_{O_3}) + \delta^2(\tau_{NO_2}) + \delta^2(\tau_{H_2O})} \tag{A7}$$

In order to obtain an approximate estimate for $\delta(\tau_{aer})$ we set $\frac{\delta(CN_0)}{\langle CN_0 \rangle} = 0.025$, (Sect. 4.2, for a link between differential error in C and CN_0 see Sect. A1) $\delta(CN) = 1$, a minimum value for $\langle CN \rangle$ of 75, $\delta(\tau_{O_3}) = 0.004$, and $\delta(\tau_{NO_2}) = 0.003$ (Sect. 4.3.1). This then yields a total estimated error of;

$$\delta(\tau_{aer}) \sim \sqrt{\left(\frac{1}{m}\right)^2 \left\{ (0.025)^2 + \left(\frac{1}{75}\right)^2 \right\} + 0.004^2 + 0.003^2} \tag{A8}$$

This yields OSM error estimates of $\delta(\tau_{aer})$ of 0.03 for $m = 1$ and (τ_{aer}).

A1 AOD error in terms of the magnitude calibration constant (C)

Equation (10), written in terms of irradiances is;

$$C = M_0^* - M_0 = -2.5 \log \frac{F_0^*}{F_0} = -k \ln \frac{F_0^*}{F_0} = k \ln \frac{F_0}{F_0^*}$$

AMTD
8, 2013–2065, 2015

where the symbol F represents an irradiance dependent quantity (i.e. digital counts, CN, in the case of the starphotometer) and $k = 2.5 \times \log(e) \cong 1.086$. The above expression underscores that the constancy of C (meaning it is only a function of the optics of the system) translates into a fixed starphotometer-irradiance to star-catalog-irradiance transformation ratio, viz;

$$\frac{F_0}{F_0^*} = K, \quad \text{where } C = k \ln K$$

Accordingly a differential (error) in C can be expressed as;

$$\mathrm{d}C = k \, \mathrm{d} \ln \frac{F_0}{F_0^*} = k \left(\frac{\mathrm{d}F_0}{F_0} - \frac{\mathrm{d}F_0^*}{F_0^*} \right)$$

If we assume that the error of the star catalog fluxes are relatively small then expression becomes;

$$\mathrm{d}C = k \frac{\mathrm{d}F_0}{F_0}$$

so that $\frac{\mathrm{d}F_0}{F_0}$ $\left(\frac{\mathrm{dCN}_0}{\mathrm{CN}_0}\right)$ can be replaced by $\frac{\mathrm{d}C}{k}$ in Eq. (A6) (and by a similar argument, $\frac{\mathrm{d}F}{F}$ $\left(\frac{\mathrm{dCN}}{\mathrm{CN}}\right)$ can be replaced by $\frac{\mathrm{d}C}{k}$) to arrive at the RMS Eq. (A7) expressed in terms of the mean square error in C.

Acknowledgements. We would like to thank NSERC (National Sciences and Engineering research Council), CFCAS (Canadian Foundation for Climate and Atmospheric Sciences), the Canadian Space Agency (CSA), CFI (Canadian Foundation for Innovation), the NSERC CREATE project (CREATE-AAS) and FQRNT (Fonds québécois de la recherche sur la nature et les technologies) for their financial support. The contributions of the CANDAC-PEARL ops team are gratefully acknowledged. We are thankful to Thomas Baader from Baader Planetarium GmbH who has kindly loaned an AZ2000 mount for the Barrow 2013 field campaign. We also appreciate the support of Matthew Martinsen and Shannon Coykendall while being on-site at Barrow.

AMTD

8, 2013–2065, 2015

References

Alados-Arboledas, L., Müller, D., Guerrero-Rascado, J. L., Navas-Guzmán, F., Pérez-Ramírez, D., and Olmo, F. J.: Optical and microphysical properties of fresh biomass burning aerosol retrieved by Raman lidar, and star-and sun-photometry, Geophys. Res. Lett., 38, L01807, doi:10.1029/2010GL045999, 2011.

Alekseeva, G. A., Arkharov, A. A., Galkin, V. D., Hagen-Thorn, E. I., Nikanorova, I. N., Novikov, V. V., Novopashenny, V. B., Pakhomov, V. P., Ruban, E. V., and Shchegolev, D. E.: The Pulkovo spectrometric catalog of bright stars in the range from 320 to 1080 nm, Balt. Astron., 5, 603–838, 1996.

Ansmann, A. and Müller, D.: Lidar and atmospheric aerosol particles, in: Lidar – Range-Resolved Optical Remote Sensing of the Atmosphere, edited by: Weitkamp, C., Springer Science + Business Media Inc., New York, 456 pp., 2005.

Ansmann, A., Wandinger, U., Riebesell, M., Weitkamp, C., and Michaelis, W.: Independent measurement of extinction and backscatter profiles in cirrus clouds by using a combined Raman elastic-backscatter lidar, Appl. Optics, 31, 7113, doi:10.1364/AO.31.007113, 1992.

ASDC: CALIPSO Quality Statements: Lidar Level 2 Cloud and Aerosol Profile Products Version Releases: 3.01, 3.02, distributed by Atmospheric Science Data Center, 2013.

Baibakov, K.: Characterization of Night-Time Aerosols Using Starphotometry, MSc thesis, University of Sherbrooke, 2009.

Barreto, A., Cuevas, E., Damiri, B., Guirado, C., Berkoff, T., Berjón, A. J., Hernández, Y., Almansa, F., and Gil, M.: A new method for nocturnal aerosol measurements with a lunar photometer prototype, Atmos. Meas. Tech., 6, 585–598, doi:10.5194/amt-6-585-2013, 2013.

Berkoff, T. A., Sorokin, M., Stone, T., Eck, T. F., Hoff, R., Welton, E., and Holben, B.: Nocturnal aerosol optical depth measurements with a small-aperture automated photometer using the moon as a light source, J. Atmos. Ocean. Tech., 28, 1297–1306, doi:10.1175/JTECH-D-10-05036.1, 2011.

Bradley, R. S., Keimig, F. T., and Diaz, H. F.: Climatology of surface-based inversions in the North American Arctic, J. Geophys. Res.-Atmos., 97, 15699–15712, doi:10.1029/92JD01451, 1992.

Carswell, A. I.: Lidar measurements of the atmopshere, Can. J. Phys., 61, 378–395, 1983.

AMTD
8, 2013–2065, 2015

Synchronous starphotometry and lidar measurements at Eureka

K. Baibakov et al.

Curry, J. A., Meyer, F. G., Radke, L. F., Brock, C. A., and Ebert, E. E.: Occurrence and characteristics of lower tropospheric ice crystals in the arctic, Int. J. Climatol., 10, 749–764, doi:10.1002/joc.3370100708, 1990.

Duarte, C. M., Lenton, T. M., Wadhams, P., and Wassmann, P.: Abrupt climate change in the Arctic, Nat. Clim. Chang., 2, 60–62, doi:10.1038/nclimate1386, 2012.

Engvall, A.-C., Ström, J., Tunved, P., Krejci, R., Schlager, H., and Minikin, A.: The radiative effect of an aged, internally mixed Arctic aerosol originating from lower-latitude biomass burning, Tellus B, 61, 677–684, doi:10.3402/tellusb.v61i4.16864, 2009.

Frohlich, C. and Shaw, G. E.: New determination of Rayleigh scattering in the terrestrial atmosphere, Appl. Optics, 19, 1773–1775, 1980.

Herber, A., Thomason, L. W., Gernandt, H., Leiterer, U., Nagel, D., Schulz, K.-H., Kaptur, J., Albrecht, T., and Notholt, J.: Continuous day and night aerosol optical depth observations in the Arctic between 1991 and 1999, J. Geophys. Res.-Atmos., 107, AAC6.1–AAC6.13, doi:10.1029/2001JD000536, 2002.

Hoffmann, A., Ritter, C., Stock, M., Maturilli, M., Eckhardt, S., Herber, A., and Neuber, R.: Lidar measurements of the Kasatochi aerosol plume in August and September 2008 in Ny-Ålesund, Spitsbergen, J. Geophys. Res., 115, D00L12, doi:10.1029/2009JD013039, 2010.

Inoue, J., Liu, J., Pinto, J. O., and Curry, J. A.: Intercomparison of Arctic Regional Climate Models: Modeling Clouds and Radiation for SHEBA in May 1998, J. Climate, 19, 4167–4178, doi:10.1175/JCLI3854.1, 2006.

Intrieri, J. M. and Shupe, M. D.: Characteristics and radiative effects of diamond dust over the western Arctic Ocean region, J. Climate, 17, 2953–2960, doi:10.1175/1520-0442(2004)017<2953:CAREOD>2.0.CO;2, 2004.

Ivanescu, L., O'Neill, N. T., Blanchet, J.-P., Baibakov, K., and Duck, T.: Star-photometers and Ground-based Lidars to evaluate Caliop during the Arctic night, Cloudsat/CALIPSO Science Team Meeting, Montreal, Canada, 2011.

Ivanescu, L., et al.: Star-photometry challenges: background artifacts and calibration aspects, in preparation, 2015.

Jacob, D. J., Crawford, J. H., Maring, H., Clarke, A. D., Dibb, J. E., Emmons, L. K., Ferrare, R. A., Hostetler, C. A., Russell, P. B., Singh, H. B., Thompson, A. M., Shaw, G. E., McCauley, E., Pederson, J. R., and Fisher, J. A.: The Arctic Research of the Composition of the Troposphere from Aircraft and Satellites (ARCTAS) mission: design, execution, and first results, Atmos. Chem. Phys., 10, 5191–5212, doi:10.5194/acp-10-5191-2010, 2010.

AMTD

8, 2013–2065, 2015

Kattsov, V. M. and Källén, E.: 4. Future climate change: modeling and scenarios for the Arctic, in: Arctic Climate Impact Assessment, Cambridge University Press, Cambridge, UK and New York, NY, USA, 2005.
Kerzenmacher, T. E.: Measurements of O_3, NO_2 and temperature during the 2004 Canadian Arctic ACE Validation Campaign, Geophys. Res. Lett., 32, L16S07, doi:10.1029/2005GL023032, 2005.
Klett, J. D.: Stable analytical inversion solution for processing lidar returns, Appl. Optics, 20, 211–20, doi:10.1364/AO.20.000211, 1981.
Leiterer, U., Naebert, A., Naebert, T., and Alekseeva, G.: A new star photometer developed for spectral aerosol optical thickness measurements in Lindenberg, Contrib. Atmos. Phys., 68, 133–141, 1995.
Lesins, G., Bourdages, L., Duck, T. J., Drummond, J. R., Eloranta, E. W., and Walden, V. P.: Large surface radiative forcing from topographic blowing snow residuals measured in the High Arctic at Eureka, Atmos. Chem. Phys., 9, 1847–1862, doi:10.5194/acp-9-1847-2009, 2009.
Lesins, G., Duck, T. J., and Drummond, J. R.: Climate trends at Eureka in the Canadian high arctic, Atmos. Ocean, 48, 59–80, doi:10.3137/AO1103.2010, 2010.
Manney, G. L., Santee, M. L., Rex, M., Livesey, N. J., Pitts, M. C., Veefkind, P., Nash, E. R., Wohltmann, I., Lehmann, R., Froidevaux, L., Poole, L. R., Schoeberl, M. R., Haffner, D. P., Davies, J., Dorokhov, V., Gernandt, H., Johnson, B., Kivi, R., Kyro, E., Larsen, N., Levelt, P. F., Makshtas, A., McElroy, C. T., Nakajima, H., Parrondo, M. C., Tarasick, D. W., von der Gathen, P., Walker, K. A., and Zinoviev, N. S.: Unprecedented Arctic ozone loss in 2011, Nature, 478, 469–475, doi:10.1038/nature10556, 2011.
McFarquhar, G. M., Ghan, S., Verlinde, J., Korolev, A., Strapp, J. W., Schmid, B., Tomlinson, J. M., Wolde, M., Brooks, S. D., Cziczo, D., Dubey, M. K., Fan, J., Flynn, C., Gultepe, I., Hubbe, J., Gilles, M. K., Laskin, A., Lawson, P., Leaitch, W. R., Liu, P., Liu, X., Lubin, D., Mazzoleni, C., Macdonald, A.-M., Moffet, R. C., Morrison, H., Ovchinnikov, M., Shupe, M. D., Turner, D. D., Xie, S., Zelenyuk, A., Bae, K., Freer, M., and Glen, A.: Indirect and Semi-direct Aerosol Campaign, B. Am. Meteorol. Soc., 92, 183–201, doi:10.1175/2010BAMS2935.1, 2010.
Moritz, R. E., Bitz, C. M., and Steig, E. J.: Dynamics of recent climate change in the Arctic, Science, 80, 1497–1502, doi:10.1126/science.1076522, 2002.
Nott, G. J., Duck, T. J., Doyle, J. G., Coffin, M. E. W., Perro, C., Thackray, C. P., Drummond, J. R., Fogal, P. F., McCullough, E., and Sica, R. J.: A remotely operated lidar for aerosol, temper-

ature, and water vapor profiling in the high Arctic, J. Atmos. Ocean. Tech., 29, 221–234, doi:10.1175/JTECH-D-11-00046.1, 2012.

O'Neill, N. T.: On NO_2 optical depths in the visible, Internal AERONET memo, GSFC/NASA, 1999.

O'Neill, N. T., Eck, T. F., Smirnov, A., Holben, B. N., and Thulasiraman, S.: Spectral discrimination of coarse and fine mode optical depth, J. Geophys. Res.-Atmos., 108, AAC8.1–AAC8.15, doi:10.1029/2002JD002975, 2003.

O'Neill, N. T., Pancrati, O., Baibakov, K., Eloranta, E., Batchelor, R. L., Freemantle, J., McArthur, L. J. B., Strong, K., and Lindenmaier, R.: Occurrence of weak, sub-micron, tropospheric aerosol events at high Arctic latitudes, Geophys. Res. Lett., 35, L14814, doi:10.1029/2008GL033733, 2008.

O'Neill, N. T., Perro, C., Saha, A., Lesins, G., Duck, T. J., Eloranta, E. W., Nott, G. J., Hoffman, A., Karumudi, M. L., Ritter, C., Bourassa, A., Abboud, I., Carn, S. A., and Savastiouk, V.: Properties of Sarychev sulphate aerosols over the Arctic, J. Geophys. Res.-Atmos., 117, D04203, doi:10.1029/2011JD016838, 2012.

Pérez-Ramírez, D., Ruiz, B., Aceituno, J., Olmo, F. J., and Alados-Arboledas, L.: Application of Sun/star photometry to derive the aerosol optical depth, Int. J. Remote Sens., 29, 5113–5132, doi:10.1080/01431160802036425, 2008a.

Pérez-Ramírez, D., Aceituno, J., Ruiz, B., Olmo, F. J., and Alados-Arboledas, L.: Development and calibration of a star photometer to measure the aerosol optical depth: smoke observations at a high mountain site, Atmos. Environ., 42, 2733–2738, doi:10.1016/j.atmosenv.2007.06.009, 2008b.

Pérez-Ramírez, D., Lyamani, H., Olmo, F. J., Whiteman, D. N., Navas-Guzmán, F., and Alados-Arboledas, L.: Cloud screening and quality control algorithm for star photometer data: assessment with lidar measurements and with all-sky images, Atmos. Meas. Tech., 5, 1585–1599, doi:10.5194/amt-5-1585-2012, 2012.

Prenni, A. J., DeMott, P. J., Kreidenweis, S. M., Harrington, J. Y., Avramov, A., Verlinde, J., Tjernström, M., Long, C. N., and Olsson, P. Q.: Can ice-nucleating aerosols affect Arctic seasonal climate?, B. Am. Meteorol. Soc., 88, 541–550, doi:10.1175/BAMS-88-4-541, 2007.

Quinn, P. K., Shaw, G., Andrews, E., Dutton, E. G., Ruoho-Airola, T., and Gong, S. L.: Arctic haze: current trends and knowledge gaps, Tellus B, 59, 99–114, doi:10.3402/tellusb.v59i1.16972, 2007.

Saha, A., O'Neill, N. T., Eloranta, E., Stone, R. S., Eck, T. F., Zidane, S., Daou, D., Lupu, A., Lesins, G., Shiobara, M., and McArthur, L. J. B.: Pan-Arctic sunphotometry during the ARCTAS-A campaign of April 2008, Geophys. Res. Lett., 37, L05803, doi:10.1029/2009GL041375, 2010.

Shaw, G. E.: Sun photometry, B. Am. Meteorol. Soc., 64, 4–10, doi:10.1175/1520-0477(1983)064<0004:SP>2.0.CO;2, 1983.

Shaw, G. E., Reagan, J. A., and Herman, B. M.: Investigations of atmospheric extinction using direct solar radiation measurements made with a multiple wavelength radiometer, J. Appl. Meteorol., 12, 374–380, 1973.

Smirnov, A., Holben, B. N., Eck, T. F., Dubovik, O., and Slutsker, I.: Cloud screening and quality control algorithms for the AERONET database, Remote Sens. Environ., 73, 337–349, 2000.

Spiegel, M. R.: Statistics, Schaum's Outline Series in Mathematics, McGraw-Hill, Toronto, 1961.

Steinbring, E., Ward, W., and Drummond, J. R.: Astronomical sky quality near Eureka, in the Canadian High Arctic, Publ. Astron. Soc. Pacific 124, no. 912, 185–194, 2012.

Stock, M., Ritter, C., Herber, A., von Hoyningen-Huene, W., Baibakov, K., Gräser, J., Orgis, T., Treffeisen, R., Zinoviev, N., Makshtas, A., and Dethloff, K.: Springtime Arctic aerosol: Smoke versus haze, a case study for March 2008, Atmos. Environ., 52, 48–55, doi:10.1016/j.atmosenv.2011.06.051, 2012.

Stone, R. S., Anderson, G. P., Shettle, E. P., Andrews, E., Loukachine, K., Dutton, E. G., Schaaf, C., and Roman, M. O.: Radiative impact of boreal smoke in the Arctic: observed and modeled, J. Geophys. Res., 113, D14S16, doi:10.1029/2007JD009657, 2008.

Stroeve, J. C., Serreze, M. C., Holland, M. M., Kay, J. E., Malanik, J., and Barrett, A. P.: The Arctic's rapidly shrinking sea ice cover: a research synthesis, Climatic Change, 110, 1005–1027, doi:10.1007/s10584-011-0101-1, 2011.

Thomason, L. W., Herman, B. M., and Reagan, J. A.: The effect of atmospheric attenuators with structured vertical distributions on air mass determinations and Langley plot analyses, J. Atmos. Sci., 40, 1851–1854, 1983.

Tomasi, C., Vitale, V., Lupi, A., Di Carmine, C., Campanelli, M., Herber, A., Treffeisen, R., Stone, R. S., Andrews, E., Sharma, S., Radionov, V., von Hoyningen-Huene, W., Stebel, K., Hansen, G. H., Myhre, C. L., Wehrli, C., Aaltonen, V., Lihavainen, H., Virkkula, A., Hillamo, R., Ström, J., Toledano, C., Cachorro, V. E., Ortiz, P., de Frutos, A. M., Blindheim, S., Frioud, M., Gausa, M., Zielinski, T., Petelski, T., and Yamanouchi, T.: Aerosols in polar regions: A

historical overview based on optical depth and in situ observations, J. Geophys. Res., 112, D16205, doi:10.1029/2007JD008432, 2007.
Verlinde, J., Harrington, J. Y., Yannuzzi, V. T., Avramov, A., Greenberg, S., Richardson, S. J., Bahrmann, C. P., McFarquhar, G. M., Zhang, G., Johnson, N., Poellot, M. R., Mather, J. H., Turner, D. D., Eloranta, E. W., Tobin, D. C., Holz, R., Zak, B. D., Ivey, M. D., Prenni, A. J., DeMott, P. J., Daniel, J. S., Kok, G. L., Sassen, K., Spangenberg, D., Minnis, P., Tooman, T. P., Shupe, M., Heymsfield, A. J., and Schofield, R.: The Mixed-Phase Arctic Cloud Experiment, B. Am. Meteorol. Soc., 88, 205–221, doi:10.1175/BAMS-88-2-205, 2007.
Wandinger, U. and Ansmann, A.: Experimental determination of the lidar overlap profile with Raman Lidar, Appl. Optics, 41, 511, doi:10.1364/AO.41.000511, 2002.
Wang, X. and Key, J. R.: Recent trends in Arctic surface, cloud, and radiation properties from space, Science, 299, 1725–1728, doi:10.1126/science.1078065, 2003.
Yamanouchi, T., Treffeisen, R., Herber, A., Shiobara, M., Yamagata, S., Hara, K., Sato, K., Yabuki, M., Tomikawa, Y., Rinke, A., Neuber, R., Schumachter, R., Kriews, M., Strom, J., Schrems, O., and Gernandt, H.: Arctic Study of Tropospheric Aerosol and Radiation (ASTAR) 2000: Arctic haze case study, Tellus B, 57, 141–152, doi:10.1111/j.1600-0889.2005.00140.x, 2005.
Young, C. L., Sokolik, I. N., and Dufek, J.: Regional radiative impact of volcanic aerosol from the 2009 eruption of Mt. Redoubt, Atmos. Chem. Phys., 12, 3699–3715, doi:10.5194/acp-12-3699-2012, 2012.

AMTD
8, 2013–2065, 2015

Table 1. Symbol and acronym glossary.

AOD	Aerosol Optical Depth [unitless]
CRL	CANDAC Rayleigh-Mie-Raman lidar
SDA	Spectral Deconvolution Algorithm
C	Starphotometry calibration constant
M	Measured star magnitude on the ground
M_0	Derived extraterrestrial instrumental star magnitude
M_0^*	Extraterrestrial star magnitude taken from the astronomical catalogue of Alekseeva et al. (1996)
m	Optical air mass
β	Backscattering coefficient (also known as the aerosol backscatter cross section) [$\mathrm{km}^{-1}\,\mathrm{sr}^{-1}$]
β_{thr}	Threshold β value used to discriminate between clouds and aerosols. Unless otherwise indicated, a nominal value of $4\times10^{-7}\,\mathrm{m}^{-1}\,\mathrm{sr}^{-1}$ was used in the event analysis of Sect. 5
S_{f}, S_{c}, S_{a}	lidar ratio (also known as the extinction to backscatter ratio) [sr] for fine mode, coarse mode and total aerosol. Prescribed values of 71 and 20 sr are employed for S_{f} and S_{c}
τ_{f}, τ_{c}, τ_{a}	fine mode, coarse mode and total aerosol optical depth derived from applying the SDA algorithm to AOD spectra from the starphotometry
τ'_{f}, τ'_{c}, τ'_{a}	fine mode, coarse mode and total aerosol optical depth derived from integrating the lidar profiles that have been partitioned into aerosol (assumed fine mode) and cloud segments using the β_{thr} classification scheme

Discussion Paper | Discussion Paper | Discussion Paper | Discussion Paper |

AMTD

8, 2013–2065, 2015

Synchronous starphotometry and lidar measurements at Eureka

K. Baibakov et al.

Table 2. Cloud filter protocol employed in this work. The three filters of the table are meant to be employed sequentially.

Filter name	Condition	Description
1. Range	$0 < \tau < 0.35$	AOD values should lie within a climatologically defined range. All the points outside the range are removed.
2. Moving slope	$a \leq 0.001\,\mathrm{min}^{-1}$	The time of each measurement is taken as a middle of a 1 h interval. The point is eliminated if the slope of the linear fit ($y = at + b$) for all measurements contained in the 1 h interval exceeds an empirically chosen threshold.
3. Outliers	$\tau - \tau_{\mathrm{avrg}} < 2.5\sigma$	A point is eliminated, if its difference relative to the average value for the whole night exceeds 2.5 standard deviations (σ). The procedure is repeated until all the differences are within 2.5σ.

AMTD
8, 2013–2065, 2015

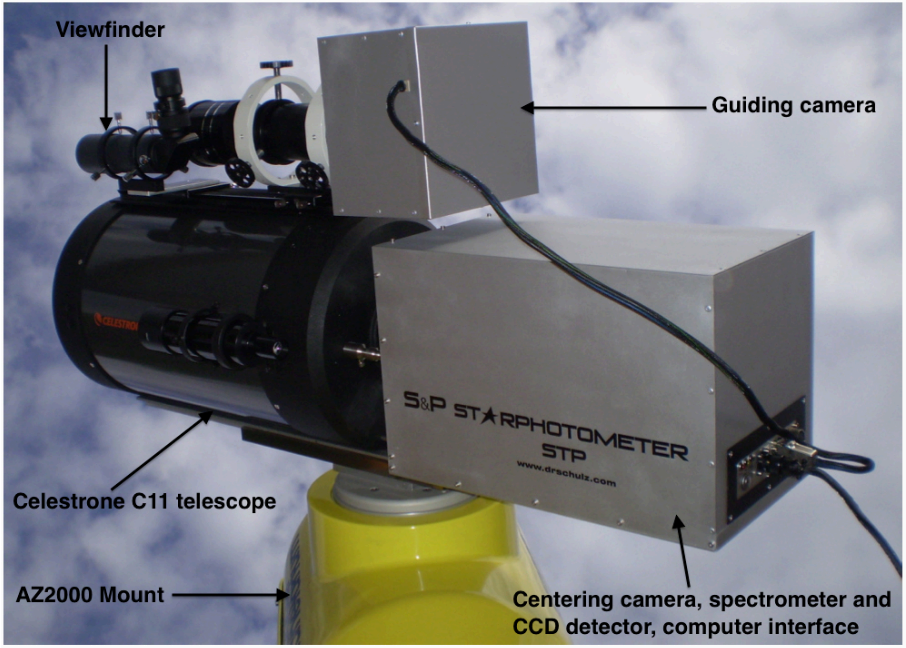

Figure 1. Principal components of SPSTAR starphotometer.

AMTD
8, 2013–2065, 2015

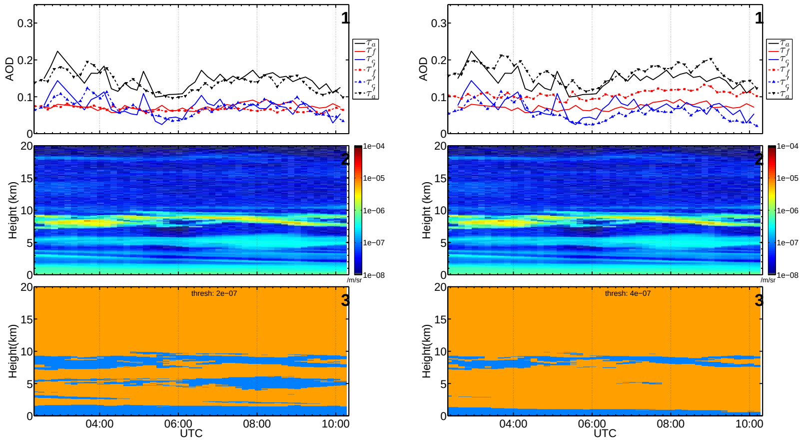

a.

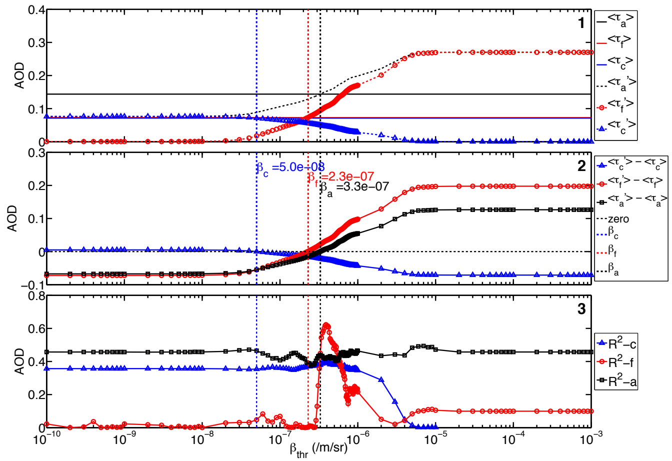

b.

AMTD
8, 2013–2065, 2015

Synchronous starphotometry and lidar measurements at Eureka

K. Baibakov et al.

Figure 2. (a) Backscatter threshold sensitivity (β_{thr}) study for the 9 March 2011 Eureka aerosol event. Panes 1: starphotometry and lidar fine and coarse mode AODs; panes 2: CRL 532 nm backscatter cross-section ($m^{-1}\,sr^{-1}$); panes 3: cloud/aerosol classification using β_{thr} values of $2 \times 10^{-7}\,m^{-1}\,sr^{-1}$ (left) and $\beta_{thr} = 4 \times 10^{-7}\,m^{-1}\,sr^{-1}$ (right). **(b)** Top graph: event-averaged lidar and starphotometer AODs as a function of the cloud discrimination threshold β_{thr}. Middle graph: differences between starphotometry and lidar event-averaged AODs. The vertical dotted lines indicate values of β_{thr} for which $\langle\tau_f\rangle = \langle\tau_f'\rangle$, $\langle\tau_c\rangle = \langle\tau_c'\rangle$ and $\langle\tau_a'\rangle = \langle\tau_a'\rangle$ respectively. Bottom graph: coefficients of determination between the lidar and starphotometry optical depths across the duration of the event.

AMTD
8, 2013–2065, 2015

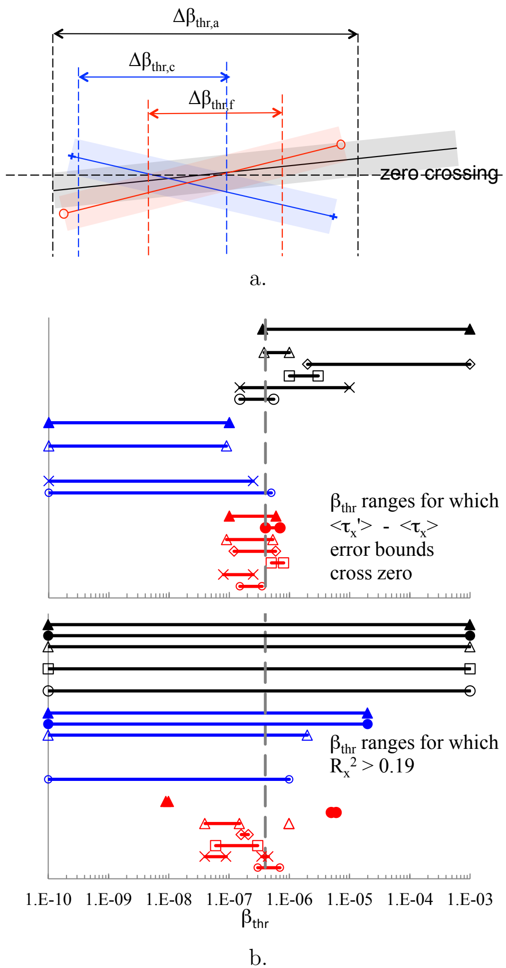

AMTD
8, 2013–2065, 2015

Synchronous starphotometry and lidar measurements at Eureka

K. Baibakov et al.

Figure 3. (a): β_{thr} ranges (dashed vertical lines) where bands of $\langle\tau_f'\rangle$–$\langle\tau_f\rangle$, $\langle\tau_c'\rangle$–$\langle\tau_c\rangle$ and $\langle\tau_a'\rangle$–$\langle\tau_a\rangle$ cross the zero line (horizontal dashed line) for an optical depth error represented by the semi-transparent bands of red, blue and grey respectively. The diagram is meant to be a conceptual representation of the analogous real data shown in the middle graph of Fig. 2b. **(b)** Top: derived β_{thr} ranges, for an assumed optical depth error of 0.03. Bottom: β_{thr} ranges for which $R_x^2 > 0.19$. The end symbols of each horizontal segment: *o*, X, □, ⋄, △, • and ▲ represent respectively, the event dates of 9 and 10 March and 21 February 2011 and 13, 14, 15 March as well as the combination of 13–15 March 2012. The grey, dashed vertical line indicates, unless otherwise stated, the nominal value of $\beta_{thr} = 4 \times 10^{-7}\ \mathrm{m^{-1}\,sr^{-1}}$ chosen for the event analyses of Sect. 5.

AMTD
8, 2013–2065, 2015

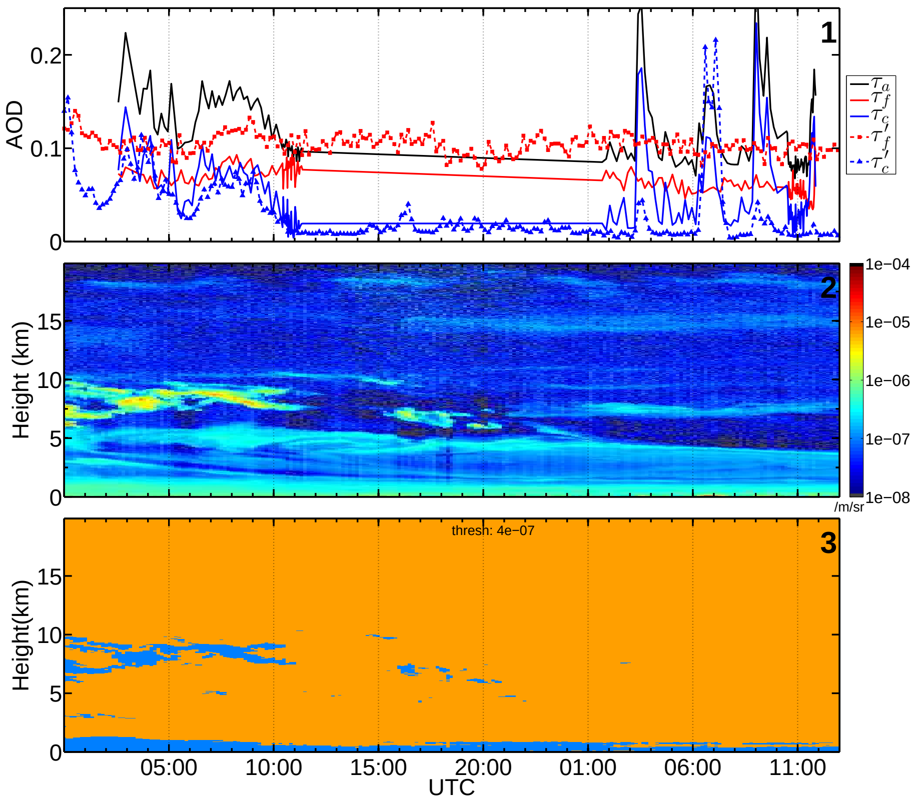

Figure 4. Eureka aerosol event, 9–10 March 2011. For a description of each pane, see the caption of Fig. 2a.

AMTD
8, 2013–2065, 2015

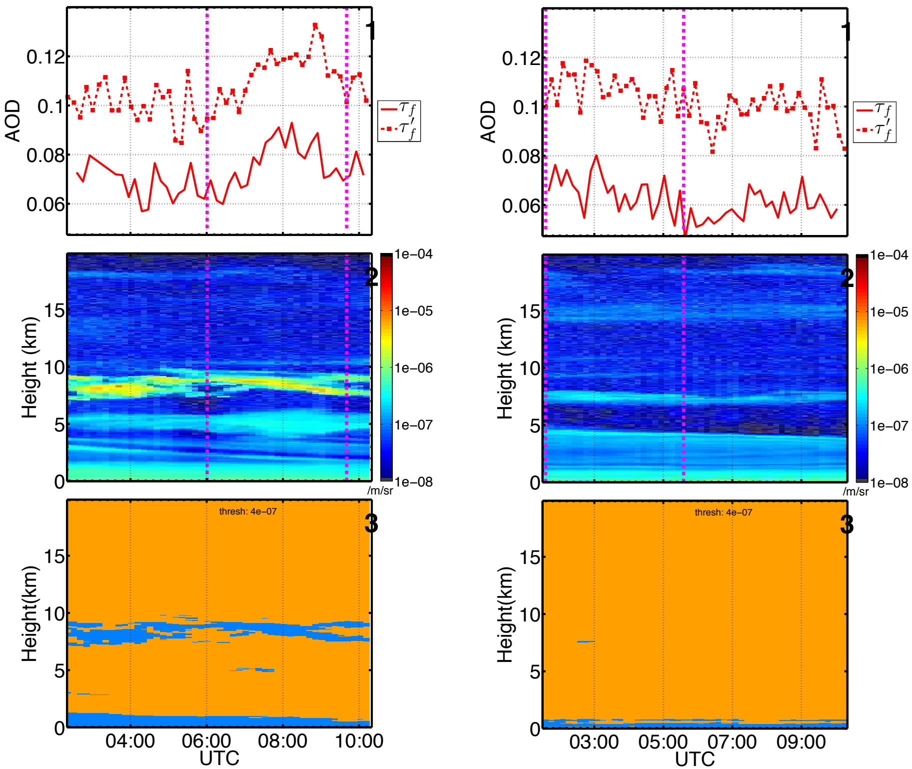

Figure 5. Zoom of the backscatter profile and the fine mode optical depths (τ_f' and τ_f) as a function of time on 9 March 2011 (left) and 10 March 2011 (right). The 9 March case is the $\beta_{thr} = 4 \times 10^{-7}\,m^{-1}\,sr^{-1}$ (right hand) case of Fig. 2a with a focus on fine mode optical depth variation. The purple dashed vertical lines show the approximate limits of where the plume (between 4 and 6 km on 9 March and at around 8 km on 10 March) is at its most optically active.

AMTD
8, 2013–2065, 2015

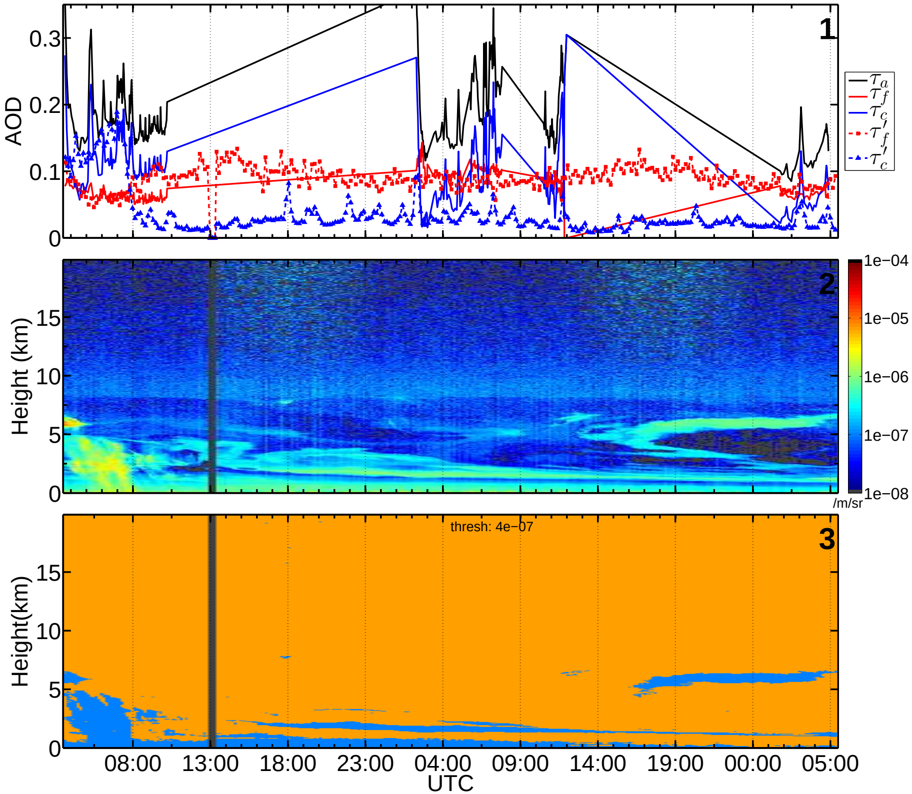

Figure 6. Same pane description as Fig. 4 but for 13–15 March 2012.

AMTD
8, 2013–2065, 2015

Synchronous starphotometry and lidar measurements at Eureka

K. Baibakov et al.

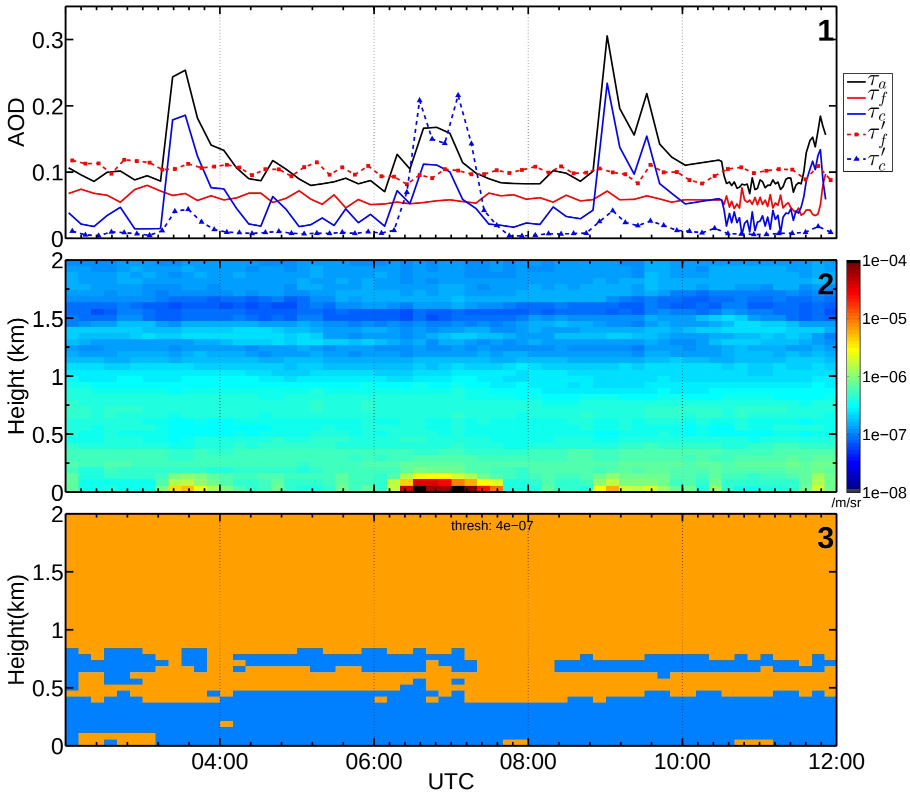

Figure 7. An altitude and temporal zoom of Fig. 4 for 10 March 2011. The CRL profiles are shown for the lowest 2 km.

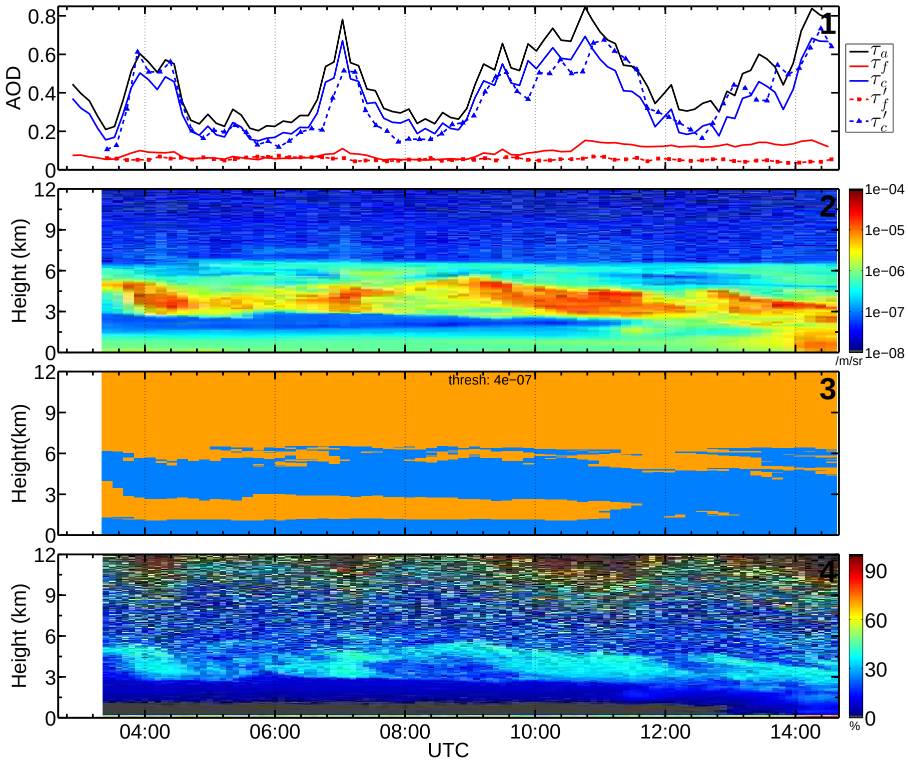

Figure 8. The description of the top 3 panes is identical to the description given in Fig. 4. Pane 4 is the CRL linear depolarization ratio (%). The data was not overlap corrected in the bottom most 1 km. Eureka, 21 February 2011.

AMTD

8, 2013–2065, 2015

Synchronous starphotometry and lidar measurements at Eureka

K. Baibakov et al.

Title Page
Abstract | Introduction
Conclusions | References
Tables | Figures
◄ | ►
Back | Close
Full Screen / Esc
Printer-friendly Version
Interactive Discussion

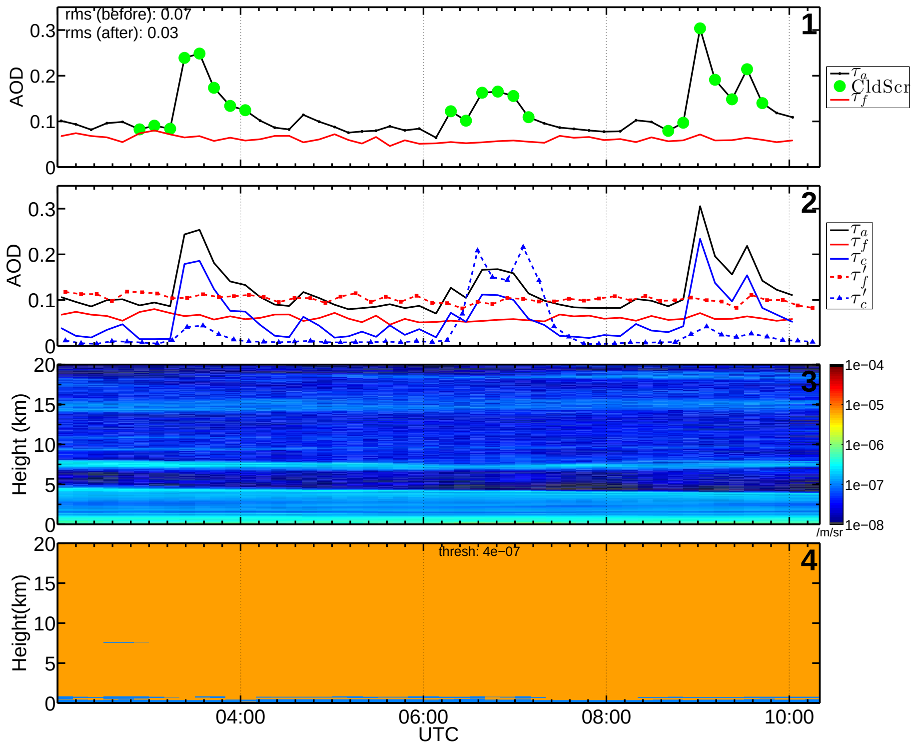

Figure 9. Pane 1: Cloud points (green circles) that would be eliminated based on a temporal cloud-screening algorithm (see text for details); fine mode starphotometry AOD (500 nm) is reproduced for ease of comparison; the description of panes 2–4 is as in Fig. 2a. 10 March 2011, Eureka.

AMTD
8, 2013–2065, 2015